

1 **Temperature and Precipitation responses to El Niño-Southern Oscillation**  
2 **in a hierarchy of datasets with different levels of observational constraints**

3 Laurence P. Garcia-Villada<sup>a,b</sup>, Markus G. Donat<sup>a,b,c\*</sup>, Oliver Angéil<sup>a,b</sup>, Andréa S. Taschetto<sup>a,b</sup>

4

5 **Affiliations:**

6 <sup>a</sup> Climate Change Research Centre, University of New South Wales, Sydney, Australia

7 <sup>b</sup> ARC Centre of Excellence for Climate Extremes, University of New South Wales, Sydney,  
8 Australia

9 <sup>c</sup> Barcelona Supercomputing Center, Barcelona, Spain

10

11 \*Correspondence to: [markus.donat@bsc.es](mailto:markus.donat@bsc.es)

12

13 **Abstract:** El Niño-Southern Oscillation (ENSO) is the dominant mode of climate variability,  
14 affecting climate conditions over large areas of the globe. There are, however, substantial  
15 differences in how ENSO teleconnections with regional climate variability are represented in  
16 different datasets such as gridded observations and climate models. Here we examine the  
17 global responses of temperature and precipitation over land to ENSO within a hierarchy of  
18 datasets with different levels of observational constraints. Anomaly maps of observed El  
19 Niño and La Niña responses are compared to reanalysis, atmospheric models driven by  
20 observed sea surface temperature (SST), and coupled atmosphere-ocean general circulation  
21 models. There is a gradual decline in anomaly pattern agreement relative to observations  
22 moving down the dataset hierarchy to lower observational constraints. We find a positive  
23 relationship between the models' fidelity in representing ENSO temperature and  
24 precipitation, though the relationship is stronger for El Niño teleconnections than La Niña.  
25 The models also reproduce El Niño response patterns with greater fidelity than La Niña  
26 patterns. Additionally, the fidelity of model-simulated responses to El Niño is related to the  
27 magnitude of SST variability in the tropical Pacific, but no such relationship could be found  
28 for La Niña responses. This comprehensive evaluation highlights the importance of  
29 realistically simulating atmospheric circulation and SST variability to better capturing the  
30 patterns of regional climate variability in response to ENSO in climate models.

31

32 **Key words:** ENSO, CMIP5, teleconnections, climate variability, model evaluation, climate  
33 models

34

## 35 **1. Introduction**

36 Recurring patterns of global precipitation and temperature have been associated with climate  
37 modes of variability that manifest via inter-annual to inter-decadal oscillations in SST.  
38 Among those modes of variability, ENSO is the dominant climate driver occurring in the  
39 tropics and affecting weather patterns in many regions of the globe. The SST patterns  
40 associated with ENSO alter the large-scale atmospheric circulation, affecting temperature and  
41 precipitation not only in the tropical Pacific but also over remote regions around the globe  
42 (Ropelewski and Halpert, 1987; Trenberth et al., 1998).

43 El Niño events are generally associated with warm/dry weather in Australia, Indonesia and  
44 northern South America and cool/wet conditions in parts of North America and the southern  
45 half of South America, whereas roughly the opposite effects are seen during La Niñas (e.g.,  
46 McPhaden et al., 2006). Predicting the climatic effects of ENSO is of crucial importance for  
47 minimizing the economic and social impacts in countries affected by its teleconnections.  
48 However, climate predictions related to ENSO are challenging as its teleconnections can be  
49 modulated by interactions with other climate drivers, including variability in the Atlantic and  
50 Indian Oceans (Cai et al., 2019). Co-occurring interactions of the Indian Ocean Dipole (IOD)  
51 and Indian Ocean basin wide warming with ENSO can modulate the strength of expected  
52 regional teleconnections in Australia, south Asia and Africa (Nicholson and Kim, 1997;  
53 Ummenhofer et al., 2009; Ummenhofer et al., 2011; Taschetto et al., 2011; Ashok et al.,  
54 2014). Similarly, rainfall response to ENSO in South America is influenced by the state of  
55 the tropical Atlantic Ocean (e.g., Rodrigues et al., 2011): El Niño-induced drying conditions  
56 in Northeast Brazil are exacerbated when the tropical North Atlantic is warmer than usual  
57 (e.g. Nobre and Shukla, 1996). Furthermore, over Australia responses to ENSO are  
58 intensified by positive and negative excursions of the Southern Annular Mode (SAM) for El  
59 Niño and La Niña respectively (Lim and Hendon 2015).

60 Furthermore, regional teleconnection responses to positive and negative ENSO phases are  
61 often non-linear and may vary through time (Hoerling et al., 1997; Power et al., 1999; Frauen  
62 et al., 2014). For example, there is an asymmetric relationship between ENSO and Australian  
63 rainfall due to low-frequency SST variations in the Pacific, such as the Inter-decadal Pacific  
64 Oscillation (IPO) (Power et al., 1999; King et al., 2013). This suggests that regional  
65 teleconnection responses to ENSO should be composited by ENSO phase to account for  
66 asymmetries in the teleconnection. While there are various reports of poor agreement

67 between simulated and observed ENSO teleconnections, most studies consider ENSO as a  
68 linear phenomenon rather than considering the teleconnections separately for each phase of  
69 ENSO. Separating teleconnection patterns by ENSO phase allows regional asymmetries in  
70 ENSO responses to be accounted for.

71 Adding to the difficulty of predicting ENSO teleconnections, climate predictions to ENSO  
72 are also challenging because it depends on the ability of climate models to realistically  
73 simulate the Pacific SST mean and variability as well as the atmosphere dynamics and  
74 thermodynamics. Global climate models display a limited capacity to reproduce ENSO  
75 teleconnections (Dieppois et al., 2015; Jourdain et al., 2013; Langenbrunner and Neelin,  
76 2013; Weare, 2012; Zou et al., 2014) due to, among other factors, biases in Pacific cold  
77 tongue and ENSO-related spatio-temporal features (e.g., Taschetto et al., 2014). Little  
78 improvement in ENSO precipitation teleconnections was found in models participating in the  
79 Coupled Model Inter-comparison Project (CMIP) phase 5 (CMIP5) compared to earlier  
80 CMIP3 models (Langenbrunner and Neelin, 2013). Weare (2012) reported that CMIP5  
81 models with better temporal ENSO characteristics tend to have teleconnections with higher  
82 spatial agreement to observations. Thus, in principle atmospheric-forced simulations, where  
83 SST biases are eliminated, could have a better representation of ENSO teleconnections than  
84 coupled climate models. However, large inter-model spread in global precipitation patterns  
85 associated with El Niños have been reported in Atmospheric Model Inter-comparison Project  
86 (AMIP) simulations (Langenbrunner and Neelin, 2013).

87 Regional evaluations have indicated weaknesses in climate models to capture the  
88 asymmetrical relationship of ENSO, for example with Australian rainfall as shown by King  
89 et al. (2015). However a systematic global evaluation of asymmetric ENSO relationships  
90 across a range of different observational and climate model datasets is missing. Interestingly,  
91 disagreements also exist among observationally constrained datasets (Bosilovich et al., 2008).  
92 For instance, Jourdain et al. (2013) concluded that a large spread among observational and  
93 reanalysis datasets was a critical challenge in their model assessment of ENSO related Indian  
94 and Australian summer monsoon rainfall. Some disagreement among previous studies could  
95 be due to differences among datasets. Therefore, analysing datasets from a hierarchy of  
96 observational constraints may help isolate where these biases are located (e.g. atmospheric  
97 circulations, oceanic ENSO simulation, etc.) and quantify the amount of disagreement each  
98 constraint reflects. This is exactly the purpose of this study: to assess ENSO teleconnections

99 using a suite of datasets following a hierarchy of observational constraints.

100 More specifically, this paper evaluates the representation of temperature and precipitation  
101 anomalies associated with ENSO across a range of different datasets. To achieve this, El  
102 Niño and La Niña anomalies are examined separately to account for asymmetries and provide  
103 simple statistical quantifications of simulated teleconnections. Using a hierarchy of datasets  
104 with different levels of observational constraints (e.g. gridded observations, reanalysis, SST-  
105 driven atmosphere general circulation models (AGCMs), and fully-coupled climate models)  
106 helps identify the steps in the hierarchy in which the simulation of regional variability  
107 deteriorates and could help diagnose sources of potential model shortcomings.

108

109

## 110 **2. Data**

### 111 **2.1 Observations**

112 We use monthly mean near surface air temperature and total precipitation from the Climate  
113 Research Unit time-series version 3.21 (CRU TS 3.21, hereafter CRU). CRU is an updated  
114 gridded dataset ( $0.5^\circ \times 0.5^\circ$ ) containing global observations from 4000 meteorological  
115 stations across the world's land areas excluding Antarctica (Harris et al. 2014). CRU contains  
116 good global coverage between the periods 1901-2012, missing data points are filled in with  
117 the climatology of the area.

118 Whilst CRU is used here as our reference data, we also assess this dataset against the  
119 following set of alternative observations: Goddard Institute for Space Studies (GISS) Surface  
120 Temperature Analysis (GISSTEMPv.5; Lenssen et al., 2019) available from 1880 to present;  
121 Hadley Centre CRU Temperature (HadCRUT4; Morice et al., 2012) from 1850 to present;  
122 Global Precipitation Climatology Centre (GPCCv.7; Schneider et al., 2011) available from  
123 1901 to present; Global Precipitation Climatology Project version 2.3 Combined Precipitation  
124 Data Set (GPCP2.3; Adler et al., 2003); and, CPC Merged Analysis of Precipitation (CMAP;  
125 Xie and Arkin, 1997), the latter two available from 1979 to present.

126 The monthly Extended Reconstructed Sea Surface Temperature version 4 (ERSST.v4)  
127 dataset (Huang et al., 2015) is used to identify El Niño and La Niña events in the  
128 observational record. ERSST.v4 contains monthly values of SST measurements reconstructed  
129 from in situ buoy and ship observations into a  $2^\circ \times 2^\circ$  longitude-latitude grid from the years

130 1875 to present.

## 131 **2.2 Reanalysis**

132 Retrospective-analysis or *reanalysis* assimilate irregular inputs of meteorological  
133 observations into a background forecast model to generate gridded output data representative  
134 of the real world's climate that may otherwise not easily be observed. We use the European  
135 Centre for Medium-Range Weather Forecasts (ECMWF) 'twentieth century reanalysis'  
136 (ERA-20C) (Poli et al., 2016) for our comparative reanalysis product.

137 The ERA-20C reanalysis assimilates surface pressure and marine winds which should enable  
138 it to reproduce observed synoptic conditions, and it further uses observed boundary  
139 conditions of SST, sea ice cover, atmospheric composition changes and solar flaring (Poli et  
140 al., 2016). While other modern reanalyses assimilate a substantially larger set of observations  
141 (e.g. Dee et al. 2011; Kanamitsu et al. 2002), we chose to use ERA-20C for this comparison  
142 because it covers a favourably extensive time period from 1900-2010 and thereby allows to  
143 investigate long-term variability more robustly compared to modern reanalyses that generally  
144 only start in 1979. More than that, ERA-20C is particularly well suited for our study since  
145 ECMWF also provides a set of SST-driven AGCM simulations with the same atmosphere  
146 model as used for the reanalysis, named ERA-20CM (Hersbach et al., 2015). Thus deviations  
147 between ERA-20C and ERA-20CM can be more directly accounted to the difference in their  
148 observational constraints; i.e. the assimilation of synoptic atmospheric conditions versus  
149 freely evolving atmospheric simulations in response to SSTs.

150 In addition to ERA-20C, we provide a comparison of the performance of this dataset with  
151 other reanalysis: 1979-present ERA5 (C3S, 2017), 1958-present Japanese 55-year Reanalysis  
152 (JRA55; Kobayashi et al., 2015) and 1948-present National Centers for Environmental  
153 Prediction / National Center for Atmospheric Research (NCEP/NCAR; Kalnay et al. 1996).

## 154 **2.3 Atmospheric models driven by observed SST**

155 The ERA-20CM dataset contains an ensemble of ten simulations covering the 1900-2010  
156 period integrated with external forcing similar to those of CMIP5, such as solar forcing,  
157 greenhouse gases (GHG), ozone and aerosols. In addition, ERA-20CM uses the same  
158 observed SST and sea ice boundary conditions as ERA-20C, i.e. the HadISST2 version  
159 2.1.0.0 (HadISST2) 0.25° x 0.25° gridded dataset (Hersbach et al., 2015). Therefore, ERA-

160 20CM also captures the occurrence of major climate events, such as ENSO and volcanic  
161 eruptions (Hersbach et al., 2015).

162 Additional SST-driven AGCM runs used in this study are experiments derived from the  
163 atmospheric components of a subset of CMIP models (Gates et al., 1999). AMIP phase 5  
164 (AMIP5) runs contain the same forcing as their CMIP5 counterparts, including prescribed  
165 GHG emissions. However, AMIP runs do not contain a simulated ocean component and are  
166 therefore constrained by prescribed observed SST and sea ice concentrations. We use 29  
167 AMIP models (Table 1) in our model hierarchy, at the same level as ERA-20CM,  
168 representing atmospheric model simulations driven by observed ocean boundary conditions.

## 169 **2.4 CMIP5**

170 We use a total of 121 historical simulations from 43 CMIP5 models which provide  
171 transiently forced simulations from the year 1850 or 1860 through to 2005 (Table 1). Long-  
172 term ‘historical’ simulations in CMIP5 are not constrained to observations, except for  
173 observed natural and anthropogenic external forcing (e.g. solar variations, volcanic aerosols,  
174 GHG). Thus, internal variability within CMIP5 runs (such as ENSO) has no temporal  
175 reference to real world events.

176 The analyses are performed over the time period 1945-2005, which is defined by the common  
177 data period of observations with reasonable spatial coverage, reanalysis and the historical  
178 CMIP model simulations. The 60-year period gives a good sample of well documented  
179 ENSO events and should allow a reasonably robust analysis of ENSO-related temperature  
180 and precipitation anomalies. AMIP runs from most models are only available from 1979-  
181 2010, so analyses are also performed for the shorter common period 1979-2005 for possible  
182 comparison with CMIP5 simulations. Additionally, one CMIP5 model, GISS-E2-R, provides  
183 longer AMIP5 runs that allow for a consistent ENSO comparison over the 1945-2005 period.

## 184 **3. Methods**

185 We classify warm and cold ENSO phases from monthly SST data within the Niño3.4 region  
186 (5°N-5°S, 120°-170°W) using the standard Oceanic Niño Index (ONI), commonly used at the  
187 National Oceanic and Atmospheric Administration (NOAA). The ONI is calculated based on  
188 a three month running mean of SST anomalies that deviate from a 30-year average  
189 climatology in the Niño3.4 region. El Niño and La Niña events are identified by ONI values

190 exceeding a threshold of +/- 0.5°C (~1.5 standard deviations) from the average climatology  
191 for at least five consecutive months. To account for long-term warming trends, we calculate  
192 ONI values from an evolving climatology using multiple centred 30-year base periods shifted  
193 every 5 years as used by NOAA<sup>1</sup>. We define an ‘ENSO year’ starting in May of an onset  
194 event and ending in April of the following year, since ENSO peaks between November-  
195 February when the ONI values are strongest.

196 ENSO years between 1945-2005 are derived from ERSST.v4 to identify ENSO events for the  
197 analysis of observations, ERA-20C and AMIP runs. However, ERA-20CM ENSO years are  
198 calculated using ocean data from the ten different realisations of HadISST2 used as boundary  
199 conditions for the different ERA-20CM ensemble members. As the ENSO year runs from  
200 May to April, our chosen time period becomes a 60-year sample size (i.e., May 1945 to April  
201 2004). The El Niño events (i.e., year of onset of the events) selected in ERSST.v4 are 1945,  
202 1951, 1953, 1957, 1958, 1963, 1965, 1968, 1969, 1972, 1976, 1977, 1982, 1986, 1987, 1991,  
203 1994, 1997, 2002, 2004; while the La Niña events are 1949, 1950, 1954, 1955, 1964, 1967,  
204 1970, 1971, 1973, 1974, 1975, 1984, 1988, 1995, 1998, 1999, 2000. Those events are the  
205 same years classified by NOAA ONI<sup>2</sup>. For individual CMIP5 runs, ENSO years are extracted  
206 from each run’s specific SST simulation. SST variability in each CMIP5 model can  
207 significantly differ from observations. Therefore, ONI values must exceed a model-run-  
208 dependent climatological threshold that is calculated, based on the runs internal SST  
209 variability, to match the equivalent ~1.5 standard deviation of NOAA’s threshold. Note that  
210 ENSO years derived from different HadISST2 ensemble members for ERA-20CM are also  
211 based on run-dependent thresholds, though these are very close to the ERSST.v4 threshold.

212

213 Prior to any calculations, all temperature and precipitation data are remapped to a common  
214 2.5° x 2.5° spatial resolution for consistency in our comparisons and to mask over the oceans  
215 and Antarctica as the focus of this study is on ENSO responses over land. We examine  
216 regional ENSO temperature and precipitation responses through composite anomaly patterns  
217 for El Niños and La Niñas (instead of linear regression analysis) to account for asymmetries  
218 in ENSO responses for the different phases of ENSO.

219

---

<sup>1</sup> [http://origin.cpc.ncep.noaa.gov/products/analysis\\_monitoring/ensostuff/ONI\\_change.shtml](http://origin.cpc.ncep.noaa.gov/products/analysis_monitoring/ensostuff/ONI_change.shtml)

<sup>2</sup> [https://origin.cpc.ncep.noaa.gov/products/analysis\\_monitoring/ensostuff/ONI\\_v4.shtml](https://origin.cpc.ncep.noaa.gov/products/analysis_monitoring/ensostuff/ONI_v4.shtml)

220 ENSO-year averages are calculated using May to April monthly average temperature and  
221 monthly-precipitation totals. We then composite the May-April years by El Niño, La Niña or  
222 Neutral phases ENSO years. For comparison, we also aggregated the temperature and  
223 precipitation means data only over the ENSO peak season (November-February), which  
224 showed similar, but stronger regional anomalies compared to annual aggregations. El Niño  
225 minus Neutral and La Niña minus Neutral fields are taken for the resulting composite  
226 anomaly maps (see section 4.1). We test whether the composites of El Niño and Neutral years  
227 (and accordingly La Niña and Neutral years) are statistically significantly different locally at  
228 each grid cell, using the Kolmogorov–Smirnov (KS) test. This test was chosen to avoid the  
229 assumption of a Gaussian distribution, which in particular for precipitation may not be  
230 fulfilled.

231

232 To provide a quantitative measure of how similar the ENSO composite patterns are between  
233 the differently constrained datasets and the observations, we calculate spatial pattern  
234 correlations of the anomaly maps using Spearman’s rank correlations (Wilks, 1995).  
235 Spearman correlation avoids assumptions of normality in the data’s distribution and is  
236 insensitive to values with large variance and amplitudes that are characteristic of climate  
237 variables. The spatial correlations are calculated for the entire hierarchy of datasets, so that  
238 each model’s run has a correlation coefficient comparing its composite patterns to the  
239 observations. We also compare the ERA-20CM, AMIP5 and CMIP5 composites to ERA-20C  
240 in addition to observations. For models where multiple realisations are available we  
241 additionally calculate concatenated model mean composites for comparison, by  
242 concatenating ENSO years among model realisations into a lengthy time series.

243

244 Pattern correlations are calculated over the 40°N to 40°S (40NS) latitude range, to avoid  
245 issues of over-weighting anomalies in high-latitude grid cells that only represent relatively  
246 small spatial areas. Furthermore, most ENSO-related responses occur in these low to mid  
247 latitudes, whereas higher latitudes are more likely affected by other climate modes and  
248 atmospheric noise. However, when calculating the pattern correlations based on global maps  
249 (i.e. 90°N-90°S, not shown) our results were qualitatively very similar to 40°N-40°S regions  
250 (see Table 2), but with correlation values on average about 0.1 lower for the global maps. We  
251 use the derived spatial correlations as a measure of model skill and compare these  
252 systematically across the hierarchy of datasets.

253

254 To calculate the significance of spatial correlations between models and observations, we  
255 take into account the climatic influence across neighbouring grid cells and reduce the  
256 effective sample size of the correlations based on the auto-correlation in the observed  
257 anomaly fields. The effective sample size is given by the equation:

258

$$259 \quad N' = N * (1 - r1)/(1 + r1),$$

260

261 where N is the sample size, N' is the effective sample size, and r1 is the first-order  
262 auto-correlation coefficient (Zwiers and von Storch, 1995). This effective sample size is used  
263 to determine the level at which pattern correlations are considered significant (e.g. red lines  
264 in Fig 5,6,8,9).

265 The correlation analysis is repeated only for regions (i.e., grid cells) that displayed a  
266 statistically significant response to ENSO in CRU. Aside from generally higher correlation  
267 coefficients, we found these results (see Fig S1-S2) for the most part displayed a similar  
268 pattern of agreement moving down the dataset hierarchy to correlations containing non-  
269 significant areas.

270

## 271 **4. Regional responses of temperatures and precipitation**

### 272 **4.1 Spatial patterns of ENSO responses**

273 The composite patterns of mean temperature and precipitation during 1945-2005 El Niño and  
274 La Niña phases are presented in the anomaly maps of Figures 1-4. Observations during El  
275 Niño years show significant warm temperature anomalies over the northern half of South  
276 America, parts of Southeast Asia and Africa (Fig 1a). Cool anomalies during El Niño are  
277 experienced over central North America but are only significant over Argentina and areas in  
278 northern and eastern Russia. Conversely, during La Niña years, most of the global land areas  
279 experience cool temperature anomalies with significant differences mainly found over the  
280 western coastal areas of North America and South America, parts of Africa, India and over  
281 some Pacific island nations (Fig 1b).

282

283 Observed precipitation composite patterns during El Niño (Fig 2a) show significantly drier  
284 conditions over Australia, the Maritime continent, Southeast Asia and Pacific islands and  
285 significantly wetter conditions on the US east coast. Rainfall anomalies over South America

286 and New Zealand show a significant dipole like response of drier anomalies over the northern  
287 regions, but wetter anomalies over southern regions. La Niña composites (Fig 2b) display a  
288 reversed response over South America, with significant wet anomalies over northern regions,  
289 but drier conditions experienced in the central and southern half of the continent.

290 Significantly wetter conditions prevail over the Maritime continent, the east coast of  
291 Australia and South Africa where monthly mean anomalies can reach more than 30mm (Fig  
292 2b).

293

294 The ERA-20C reanalysis reproduces the observed patterns of regional anomalies very well  
295 (Fig 1-2, c-d). The anomalies can slightly deviate from observations over some regions,  
296 however these are very minor. For example, exaggerated El Niño and underestimated La  
297 Niña temperature anomalies over Alaska (Fig 1c and 1d) and opposite signed precipitation  
298 patterns during La Niña over south east Asia (Fig 2d). For the most part, ERA-20C captures  
299 the location of significant hatching in the observations and its anomaly patterns are highly  
300 correlated to CRU for both phases of ENSO. Although quantitatively, El Niño patterns  
301 display a higher agreement to observations than La Niña patterns (Table 2).

302

303 The anomaly patterns produced by the ERA-20CM ensemble mean also displays strong  
304 similarity to the observed and reanalysis composites. The broad temperature patterns are well  
305 captured and the strongest precipitation anomalies are correctly located over South America  
306 and the Maritime continent (Fig 1e-f, 2e-f). Precipitation patterns display only minor  
307 differences in the strength, location and sign of regional anomalies (Fig 2e-f and 2a-b).

308 Additionally, regions with significant anomalies in the ensemble mean are located in similar  
309 regions to CRU and ERA-20C, though with larger significant areas. In particular the  
310 Northern Hemisphere extra-tropics show a large ensemble standard deviation for temperature  
311 anomalies (Figure 1g, h), highlighting the role of atmospheric variability across the 10 ERA-  
312 20CM ensemble members.

313

314 ERA-20CM ensemble mean correlations (Table 2) for temperature (0.45-0.63) and  
315 precipitation (0.59-0.66) with CRU are moderate, but anomaly patterns are in slightly higher  
316 agreement with ERA-20C (Table 3). Regions within ERA-20CM that show the strongest  
317 anomalies are those where internal variability and standard deviations are larger. For  
318 temperature anomalies the largest spread is found in the northern hemisphere (Fig 1g-h) and

319 for precipitation anomalies throughout 40NS latitudes mostly over the regions of Southeast  
320 Asia and the Maritime Continent (Fig 2g-h).

321

322 CMIP5 models reproduce composites of ENSO anomalies with wide ranging agreement to  
323 observations; as illustrated in realisations that have the highest, median and lowest correlation  
324 with CRU (Fig 3-4). The ‘best’ individual simulations (measured by their spatial correlation  
325 with CRU) display broad patterns of regional temperature and precipitation anomalies with  
326 striking resemblance of the observations (Fig 3a/b and 4a/b). However, El Niño anomalies  
327 appear to be much stronger in CMIP5 than represented in the observations (Fig 3a and 4a).  
328 Whereas La Niña anomalies display similar magnitudes to CRU but are less accurate in their  
329 pattern location (Fig 3b and 4b).

330

331 CMIP5 El Niño patterns with the highest correlations display significant relationships over a  
332 substantially larger area than seen in CRU (Fig 3a, 4a); this exaggerated significance closely  
333 resembles to ERA-20CM temperature patterns (Fig 1e, 3a), which have more significant  
334 relationships than observed among the 10 ensemble members (not shown). Quantitatively, the  
335 CMIP5 models with the highest correlated realisations, reproduce anomaly patterns with near  
336 equal performance as the ERA-20CM ensemble mean. It is possible that those CMIP5  
337 models may have a more realistic representation of the SST anomaly structure associated  
338 with ENSO or simulate a stronger coupling between the atmosphere and the ocean in the  
339 tropical Pacific or underestimate the level of internal atmospheric noise expected in the real  
340 world. Indeed, MIROC5 (Fig 3a) has been shown to simulate well the spatial pattern of SST  
341 anomalies associated with ENSO, however it overestimates the strength of El Niño events  
342 (Taschetto et al. 2014). On the other hand, HadGEM2-ES (Fig 3b) and GFDL-CM2 (Fig 4a)  
343 are able to simulate ENSO spatial characteristics within observations (Taschetto et al. 2014),  
344 which indicates that strong air-sea coupling in the equatorial Pacific is a more likely  
345 candidate to explain why correlation patterns with CRU are overestimated in these models.  
346 Interestingly, realisations of the CNRM-CM5 model are both ranked lowest for temperature  
347 (Fig 3f) and highest for precipitation (Fig 4b) during La Niña, suggesting a large spread  
348 within the model ensemble.

349

350 CMIP5 runs with poor agreement simulate anomalies with varying strength or opposite sign  
351 than observed. For example, it is interesting to note that a couple of realisations of the GISS-  
352 E2-H model rank lowest in the spatial correlation pattern with observations for both

353 temperature and precipitation (Figs 3e and 4e-f). Contrary to observations, anomalies are dry  
354 over Indonesia during La Niña (Fig 4f) and wet during El Niño (Fig 4e). The GISS-E2-H  
355 model tends to simulate overly weak ENSO-related SST anomalies (Taschetto et al. 2014),  
356 which is likely not strong enough to drive atmospheric teleconnections as observed. In  
357 addition to the weak SST forcing, biases in ENSO seasonality (i.e. variance and phase  
358 locking in Niño3 and Niño4 regions; Taschetto et al. 2014) can contribute to the lowest  
359 performance of the GISS-E2-H model. Note that the intention of discussing particular models  
360 according to their performance is to make the point that there is large diversity in the  
361 representation of ENSO teleconnections and by no means it is intended to condemn specific  
362 models. We show later that there can be a considerable spread in ENSO response across  
363 ensemble members from same model. We further examine how the various CMIP5 models  
364 compare in their El Niño and La Niña composite pattern agreement in section 4.2.

365

#### 366 **4.2 Systematic comparison of the pattern agreement of ENSO responses across different** 367 **datasets**

368 Figures 5 and 6 show the range of agreement in the ENSO composite patterns with CRU  
369 across ERA-20C, ERA-20CM and CMIP5 models. The number of markers shown for a given  
370 model represent the number of simulations analysed from that model. Figure 5 displays El  
371 Niño (Fig 5a) and La Niña (Fig 5b) temperature composite pattern agreements of models  
372 ordered from left to right by highest average correlation with CRU. The ERA-20C reanalysis  
373 displays the highest agreement for both El Niño (0.78) and La Niña (0.53) temperature  
374 composites, followed closely by MIROC5 for El Niño and the ERA-20CM mean for La  
375 Niña. The majority of the CMIP5 runs have lower agreement with CRU than ERA-20CM,  
376 with the average of temperature pattern correlations being 0.45 for El Niño and 0.25 for La  
377 Niña (see Table 2) across the CMIP5 ensemble. This confirms our hypothesis that  
378 correlations worsen as less observational constraints are considered in the simulations.  
379 Interestingly, despite the lack of observational constraints, MIROC5 reproduces higher  
380 correlation pattern with CRU than ERA-20CM.

381

382 The correlations of precipitation composites displayed in Figure 6 illustrate again a consistent  
383 deterioration of pattern agreement with CRU moving down the dataset hierarchy. ERA-20C  
384 again displays the highest correlation for El Niño (0.73) and La Niña (0.60), followed closely  
385 by the ERA-20CM mean and the ERA-20CM 10-member realisations for El Niño (0.73) and  
386 for La Niña (0.53). The average of precipitation correlations across the CMIP5 runs is

387 approximately 0.44 and 0.34 for El Niño and La Niña respectively (see Table 2), where the  
388 CMIP5 ensemble mean correlations range between approximately 0.65-0.35 for El Niño and  
389 0.50-0.30 for La Niña. The inter-model spread of precipitation correlations (Fig 6) among the  
390 different models' realisations appears to be lower in comparison to temperature correlations  
391 (Fig 5). It is interesting also to note that, despite the overall deterioration of correlations in  
392 CMIP5 models compared to observations and reanalysis, the spread across realisations of  
393 individual CMIP5 models is comparable to the spread within ERA-20CM ensemble  
394 members. This suggests that internal variability in the climate system may partially account  
395 for the diversity in ENSO teleconnections.

396

397 Interestingly, as in the reanalysis and the ERA-20CM, CMIP5 models show lower pattern  
398 correlations for La Niña anomalies compared to those during El Niño. This is likely due to  
399 the inherent nonlinear behaviour of ENSO SST pattern and atmospheric convection in the  
400 equatorial Pacific (Hoerling et al., 1997; Frauen et al., 2014). Additionally, ERA-20CM and  
401 CMIP5 models' composite patterns in most cases correlate slightly higher with ERA-20C  
402 than CRU (See Table 3). This may be because in ERA-20C temperature and precipitation are  
403 also model-simulated variables and affected by similar model biases, whereas observations  
404 may be affected by other issues such as quality and completeness of the meteorological  
405 station observations. Considering the ensemble averages for individual models (indicated by  
406 the yellow stars) where models provided multiple simulations indicates the individual model  
407 ensemble means are in most cases higher or close to the correlation of the ensemble member  
408 with highest correlation. The multi-model ensemble mean shows correlations higher than all  
409 CMIP5 models (for precipitation), or highest apart from one model with higher correlations  
410 (for temperature). This high correlation is expected since noise is attenuated by averaging  
411 over many ensemble members. For a fair comparison, we focus our discussions on the  
412 correlations of individual ensemble members instead of the multi-model means in order to  
413 keep a sound assessment across simulations of same length and similar ENSO sample.

414

415 There is a general tendency that models that simulate temperature anomaly patterns more  
416 similar to observations also have precipitation anomalies more similar to observations. Figure  
417 7 shows a strong positive relationship between CMIP5 correlations of temperature and  
418 precipitation for El Niño (Fig 7a) and La Niña (Fig 7b). The relationship is much stronger for  
419 El Niño with a correlation of 0.74 than for La Niña 0.42. This suggests that both variables are  
420 not independent of each other, which makes sense physically, as regional responses to wet

421 and cloudy conditions can lead to lower temperatures, as for example, during La Niña in  
422 eastern Australia. Warm temperature anomalies are experienced when there is less cloud  
423 cover and enhanced net radiative flux to the surface (such as those experienced in Australia  
424 during El Niño), which is usually associated with less precipitation. Additionally, strong El  
425 Niño events lead to a tropospheric warming in the tropics that leads to a more stable  
426 atmospheric environment, thus decreasing rainfall over convective regions in the tropics  
427 (Yulaeva and Wallace 1994). Therefore, given the close relationship between convection,  
428 precipitation and temperature in the tropics during ENSO years, it is perhaps not surprising  
429 that models that are able to simulate ENSO-related precipitation anomalies more accurately  
430 also represent the associated temperature response well. Note, however, that the temperature  
431 and precipitation anomaly patterns themselves are only weakly related (e.g. spatial  
432 correlations of -0.14 for the El Niño composite and -0.05 for La Niña in the 40NS domain  
433 based on CRU observational data), because the temperature response to El Niño is a  
434 widespread warming in the tropical troposphere while the rainfall responses involve  
435 dynamics to remote regions (e.g. via Walker and Hadley circulations).

436  
437 We also analyse the pattern correlations for AMIP5 simulations, to complete the hierarchy of  
438 datasets by a number of SST-driven AGCM runs (complementing the results with ERA-  
439 20CM). As most AMIP runs are available only from 1979 onwards, this analysis is  
440 performed over the shorter period 1979-2005. Anomalies and pattern correlations from the  
441 other datasets were additionally calculated over this shorter period to provide an equitable  
442 comparison across all datasets. Figures 8 and 9 show correlations of temperature and  
443 precipitation ENSO composites for the AMIP5 and subset of CMIP5 runs compared to CRU  
444 (note that the blue dots representing CMIP5 in Figures 8 and 9 differ from those data points  
445 in Figure 5 and 6 because a shorter analysis period is used in these latter Figures to match  
446 AMIP data availability).

447  
448 The ENSO composites during the shorter AMIP period again show that ERA-20C reproduces  
449 anomaly patterns with the highest agreement with CRU, in most cases followed by the ERA-  
450 20CM ensemble mean. AMIP5 runs generally show greater agreement with observations in  
451 simulating temperature and precipitation patterns for both phases of ENSO than CMIP5  
452 counterparts. The AMIP5 temperature composites correlate with CRU on average 0.45 for El  
453 Niño and 0.35 for La Niña, while CMIP5 runs on average correlate by 0.28 and 0.14  
454 respectively. AMIP5 precipitation composites correlate with CRU on average by 0.42 for El

455 Niño and 0.35 for La Niña and 0.30 and 0.23 for CMIP5 respectively. However, there are  
456 some cases where individual CMIP5 runs reproduce composites that correlate higher than the  
457 AMIP5 runs (e.g. MPI-ESM-LR in Fig 8a and b, CNRM-CM5 and CESM1 in Fig 9a).

458

459 To assess whether analyses over the 26-year AMIP period may be biased due to the smaller  
460 sample size, we also analysed a 60-year period (consistent with other analysis in this study)  
461 provided by the longer AMIP5 runs of the GISS-E2-R model. The 60-year GISS-E2-R period  
462 again for the most part display higher correlations in AMIP5 runs than their comparable  
463 CMIP5 runs (see Fig S3-S4). Although GISS-E2-R CMIP5 runs perform more similarly to  
464 AMIP runs for El Niño precipitation composites. These results confirm, as expected, that  
465 AMIP5 runs generally produce temperature and precipitation El Niño and La Niña composite  
466 patterns that are in higher agreement with observations than CMIP5 runs.

467

468 To summarise the results from the AMIP5 period, Figure 10 clearly shows a gradual  
469 deterioration in agreement with CRU moving down the hierarchy of observationally  
470 constrained datasets. Interestingly, it also shows a clear division between the models' ability  
471 to simulate temperature and precipitation responses during warm and cold phases of ENSO.  
472 In general, the models are better able to reproduce composites of El Niño patterns compared  
473 to La Niña patterns (Fig 10). Figure 11 confirms that the agreement of simulated El Niño  
474 teleconnections with observations does not depend on how La Niña teleconnection patterns  
475 are simulated in CMIP models and vice versa. In other words, there is no reason to expect  
476 that models simulating well the El Niño temperature response will also simulate well the La  
477 Niña temperature response (Fig 11a). This is also the case for ENSO precipitation  
478 teleconnections (Fig 11b).

479

480 Since CMIP5 models reproduce ENSO related temperature and precipitation responses with  
481 limited capabilities but show a wide spread in correlations, an important question to ask is  
482 whether the quality of the ENSO responses is related to certain model characteristics? In  
483 particular, we examine the possible effects of (1) SST variability in the tropical Pacific, and  
484 (2) the resolution of the atmospheric model.

485

486 Figure 12 shows the correlation of CMIP5 runs as a function of their ENSO ONI threshold  
487 value (representing the magnitude of SST variability). There is a significant positive  
488 correlation between the strength of a CMIP5 run's internal SST variability (represented here

489 by the ONI threshold) and the agreement of composited El Niño temperature  $r_s=0.61$  (Fig  
490 12a) and precipitation  $r_s=0.70$  (Fig 12c) patterns with observations. However, the correlation  
491 is much lower for La Niña temperature  $r_s =0.20$  (Fig 12b) and precipitation  $r_s=0.39$  (Fig 12d)  
492 patterns and only significant for precipitation. What is important here is that models with  
493 very low Niño3.4 SST variability show the lowest correlations for El Niño teleconnections.  
494 While this is overall also true for La Niña precipitation responses, some models produce poor  
495 La Niña temperature teleconnection agreement even with strong SST variability. This likely  
496 reflects the nonlinear response of the atmospheric convection in the equatorial Pacific during  
497 El Niño and La Niña events.

498

499 Figure 13 shows the relationship between the number of grid boxes in CMIP5 models (native  
500 atmospheric resolution) and the spatial correlation of its ENSO temperature (top row) and  
501 precipitation (bottom row) anomalies with observations. The number of blue dots is reduced  
502 here because they represent a model's average correlation, as opposed to separate correlations  
503 for each run as in the other scatter plots. This averaging is expected to reduce noise from  
504 climate variability, but even at this reduced noise level there is no clear relationship between  
505 ENSO temperature and rainfall responses and horizontal resolution of the atmosphere model.  
506 However, models with very coarse resolutions tend to have the lowest agreement of El Niño  
507 temperature and precipitation responses to observations, but this is not the case for La Niña  
508 composites. These results are similar to findings from Weare (2012) but we have extended  
509 this to La Niña phases.

510

## 511 **5. Discussion**

512

513 Regional climate in many regions of the world is modulated by ENSO. Climate models are  
514 commonly used tools to study past and future climate. However, when using models to derive  
515 regional climate information, more assurance of models realistically simulating  
516 characteristics of regional climate variability is needed. Previous studies comparing  
517 relationships of regional climate with ENSO between observations and climate models have  
518 reported uncertainties and model shortcomings. Better understanding the effects of ENSO on  
519 regional climate and related mechanisms is important because it will enable more reliable  
520 predictions of seasonal to inter-annual variability.

521 Our analysis provides a survey of the representation of global ENSO related temperature and  
522 precipitation responses over land across a hierarchy of datasets with different levels of  
523 observational constraints (e.g. gridded observations, reanalysis, AGCMs and AOGCMs) to  
524 help enable future studies to isolate potential model shortcomings at different steps of the  
525 hierarchy. We examined ENSO composited anomaly maps separately for warm and cold  
526 phases to account for asymmetric relationships. The results show a gradual decline in the  
527 pattern correlation of composited anomaly maps relative to observations (CRU) moving  
528 down the hierarchy from most to least observationally constrained models. These results are  
529 for the most part in robust agreement with analyses using only statistically significant grid  
530 cells (see Figs S1-S2).

531

532 It is important to note that observations and reanalyses can also differ considerably among  
533 each other. To show this, Figure 14 exhibits the correlation coefficients of ENSO composites  
534 using CRU against a diverse set of observations and reanalyses with different time lengths.  
535 Observational datasets of temperature (GISS and HadCRU) and precipitation (GPCC, GPCP  
536 and CMAP) reveal highest correlations with CRU ( $\sim 0.65$ - $0.85$ ; see Table 2 and 3 for details),  
537 while reanalysis datasets (ERA5, JRA55 and NCEP/NCAR) show second largest correlations  
538 coefficients ranging from  $\sim 0.20$  and  $0.85$ , followed by AMIP ( $\sim 0.4$ ) and CMIP5 models  
539 ( $\sim 0.15$  to  $0.45$ ). Despite the modest spread across observations and reanalyses, Figure 14  
540 strongly supports the results using ERA-20C and ERA-20CM.

541

542 We can therefore conclude that reanalysis composites are in the highest agreement with the  
543 observations. This is likely because ERA-20C (and the other reanalyses analysed here) is  
544 physically coherent and constrained by ocean and atmospheric observations, which helps  
545 simulate realistic synoptic systems and thereby the correct teleconnection pathways and  
546 seasonality for more accurate anomalies even over high latitudes that have less robust ENSO  
547 responses. Deviations between observations and the ERA-20C reanalysis may point to  
548 quality issues in the observations, such as the coverage and quality of meteorological stations,  
549 or resulting from unknown or poorly represented physical processes that lead to model biases  
550 (e.g. parameterisations).

551

552 ERA-20CM composites are generally in the second highest order of agreement, particularly  
553 in ensemble mean composites, by approximately  $0.05$ - $0.20$  lower spatial correlation than  
554 ERA-20C. ERA-20CM contains the same atmospheric model as ERA-20C which would

555 suggests that the representation of observed weather systems is responsible for the  
556 differences in their ENSO anomaly pattern agreement. The lower correlations in ERA-20CM  
557 can be attributed to the loss of assimilation of atmospheric observations which increases the  
558 degree of freedom in the models internal variability of the atmosphere but also gives way to  
559 typical model biases such as underestimated blocking (Scaife et al., 2010) or shifted location  
560 of storm tracks (Kidston and Gerber, 2010). The loss in correlations here is expected since  
561 there is no observational weather constraint and consequently different representations of  
562 atmospheric circulation. This illustrates that a realistic representation of both atmospheric  
563 circulation and SST variability seems necessary to realistically simulate global patterns of  
564 ENSO related temperature and precipitation anomalies. If either of these components are  
565 missing, this will lead to poorer agreement with observations.

566

567 Similarly, the decline of correlations between AMIP5 and CMIP5 coupled runs can be  
568 attributed to the introduction of a simulated ocean component. AMIP5 runs only simulate the  
569 atmospheric component of CMIP5 models, constrained by observed SST, and produce  
570 correlations on average  $\sim 0.2$  higher in agreement with CRU than the coupled CMIP5 runs  
571 (Table 2). This suggests that having a realistic ocean component leads to ENSO  
572 teleconnections with enhanced agreement with observations. A prescribed ocean also seems  
573 to constrain the simulated teleconnection pathways. This may also be due to a prescribed  
574 ocean constraining the variability of other modes of climate that can influence regional  
575 teleconnections. For example, the relationship between Indian monsoon rainfall and ENSO is  
576 modulated by the IOD (Ashok et al. 2001). Therefore, the range of inter-model correlation  
577 variability is lower in AMIP5 runs compared to CMIP5.

578

579 CMIP5 composite patterns are typically poorer in agreement with observations and have  
580 average correlations that range between approximately 0.15-0.30 lower than ERA-20C, ERA-  
581 20CM and AMIP models. The large inter-model and internal correlation differences occur for  
582 several reasons including biases in simulating mean ocean and atmosphere circulation;  
583 diversity in parameterisations among models (e.g. cloud microphysics); differences in the  
584 incorporated land models used; different ocean variability interactions occurring between  
585 inter-dependent modes of climate; and internal variability in the climate system, including a  
586 diverse range of multi-decadal variability simulated in climate models (Power et al., 2016).

587

588 ENSO teleconnections to regional climate are modulated on multi-decadal timescales by  
589 climate modes of variability such as the IPO or the Pacific Decadal Oscillation (e.g. Power et  
590 al., 1999; Andreoli and Kayano, 2005; Chan et Zhou, 2005; Yoon and Yeh, 2010; Ashok et  
591 al., 2014; Kim et al. 2014). For instance, the ENSO-Australian rainfall relationship appears to  
592 be stronger during the negative phase of the IPO (Power et al., 1999); while the ENSO-  
593 northeast Asian summer monsoon and ENSO-East Asian winter monsoon relationships are  
594 stronger when ENSO and PDO are in phase (Yoon and Yeh, 2010; Kim et al., 2014).

595

596 However, CMIP models tend to overall underestimate internal multi-decadal variability  
597 (Power et al., 2014). This could contribute to the inability of climate models to simulate the  
598 fluctuations in ENSO teleconnections and could explain the decline in correlations compared  
599 to AMIP and reanalysis that are constrained by observed SST. To add to the non-stationarity  
600 of ENSO teleconnections, the impact of ENSO on regional temperature and rainfall is also  
601 modulated by the effect of other climate drivers occurring in the Atlantic and Indian Oceans,  
602 for example the IOD and Atlantic Niños, or local SST anomalies. Therefore, a correct  
603 representation of the combined effect of ENSO and feedback from other oceanic basins is  
604 needed to capture ENSO teleconnections accurately. CMIP5 models have shown biases in  
605 inter-basin interactions, particularly in the tropical Atlantic Ocean, which has a systematically  
606 biased cooler mean state that limits the correct interaction with the Pacific variability (Kajtar  
607 et al., 2018; McGregor et al., 2018; Cai et al. 2019).

608

609 On top of natural variations in the climate system and model biases in coupled ocean-  
610 atmosphere processes, uncertainties in the patterns and strength of ENSO teleconnections can  
611 originate from different ENSO spectral behaviors simulated by climate models (Wittenberg  
612 2009) or internal atmospheric variability independent of ENSO (e.g. Deser et al., 2018).  
613 Wittenberg (2009) shows that climate models can simulate ENSO characteristics with a  
614 diversity of spectral behaviours that are modulated on multidecadal to centennial timescales.  
615 Wittenberg (2009) further demonstrates that the large variety of ENSO's spectral behavior  
616 can be explained by applying Poisson statistics to ENSO's seasonal phase locking and  
617 interannual memory associated with Pacific Ocean dynamics and modal time scales. In  
618 addition, internal atmospheric dynamics unrelated to ENSO are a factor that is commonly  
619 overlooked by many studies (e.g. Deser et al., 2018). Intrinsic atmospheric variability cannot  
620 be neglected to account for differences in the correlations seen in this study, particularly  
621 across members of the same model/reanalysis. The different simulations of ENSO behaviors

622 in CMIP models (due to stochastic atmospheric noise and/or ocean dynamics) can potentially  
623 increase the amount of spread across ensemble members thus contributing to the large  
624 diversity in the representation of temperature and precipitation teleconnections.

625

626 Nevertheless, one would expect that biases in the tropical Pacific would have a more direct  
627 effect on the climatic impacts of ENSO. There are documented weaknesses in CMIP5  
628 responses to ENSO over different regions due to poor ENSO spatial patterns and seasonality  
629 (Dieppois et al., 2015; Jourdain et al., 2013). In particular, ENSO events can manifest in  
630 distinct ‘flavours’ of spatial pattern, amplitude and temporal evolution, the two most common  
631 distinctions of ENSO ‘types’ being the Eastern Pacific (EP) events (which have SST  
632 anomalies that peak along the eastern Pacific) and the Central Pacific (CP) events (where  
633 anomalies peak near the central Pacific, see Trenberth and Stepaniak, 2001; Ashok et al.,  
634 2007; Capotondi et al., 2015). Since the atmosphere is highly responsive to the location of the  
635 SST anomalies, variations in ENSO type lead to differences in the expected atmospheric  
636 teleconnection responses (Weng et al., 2007; Ashok et al., 2007; Taschetto et al. 2009; Hill et  
637 al. 2011; Tedeschi et al., 2013; Capotondi et al., 2013; Marathe et al., 2015; Yeh et al., 2018).  
638 Weaknesses in GCM’s oceanic ENSO simulation are a common question regarding the  
639 fidelity of models.

640

641 Taschetto et al. (2014) reported that CMIP5 models represented the different phases of ENSO  
642 with varying degrees of capability. CMIP5 models can simulate the two types of El Niños,  
643 but the majority fail to capture the observed amplitude and magnitude for La Niñas. Zou et al.  
644 (2014) also found that CMIP5 models were more capable of simulating EP than CP El Niño  
645 events. In addition, they showed that CMIP5 models were more capable of realistically  
646 simulating the concomitant US regional temperature response for EP El Niño’s than for CP  
647 El Niño events. This provides further evidence that a realistic simulation of ENSO’s oceanic  
648 component is necessary for simulating more accurate teleconnections with climate variables  
649 over land. Since CMIP5 models present limitations in simulating two types of ENSO, we do  
650 not distinguish between EP and CP ENSO events, but instead use a single classification of  
651 ENSO determined by the ONI index, that captures both types of events. In addition,  
652 separating our analysis into two ENSO types would reduce the sample size considerably,  
653 particularly for the AMIP comparison that starts in 1979, thus affecting the confidence in our  
654 results. Nevertheless, this is an important point that should be considered in future studies

655 perhaps with the next generation of climate models (that hopefully simulate more realistically  
656 the diversity of ENSO) and using longer simulations to avoid issues with small sample size.

657

658 Interestingly, we find that models simulate El Niño composite patterns for both temperature  
659 and precipitation with greater fidelity than La Niña composites. This is also seen in  
660 observations and reanalysis (Fig 14). El Niño mean temperature and total precipitation  
661 correlations being approximately 0.1 higher than for La Niña composites. In nature, El Niño  
662 events generally manifest with higher amplitudes than La Niña events (Frauen and  
663 Dommenges, 2010; Burgers and Stephenson, 1999). This asymmetry can drive stronger  
664 teleconnections in models. Another possible reason for the ENSO teleconnection asymmetry  
665 relates to the region where SST anomalies develop in the Pacific (Hoerling et al., 1997). We  
666 found that El Niño composite patterns are more sensitive to the magnitude of Niño3.4 SST  
667 variability than La Niña composites patterns (Fig 12).

668

669 Atmospheric teleconnections generally occur when deep convection is triggered by warm  
670 SST (among other processes) and this depends on SST anomalies and the SST background  
671 state (or climatology). El Niño events generate warm SST anomalies to the CP and/or EP  
672 which causes atypical convection in the surrounding areas. While El Niño events can shift the  
673 center of convection, this is much subtler for La Niña events. La Niña events can be seen as  
674 an intensification of the mean state in the Pacific. As such, the center of convection  
675 associated with the upward branch of the Walker circulation does not change as much during  
676 La Niña events, neither the extension of the Pacific warm pool.

677

678 La Niña events enhance SST conditions in the Maritime Continent/western Pacific which  
679 already naturally favours deep convection. Thus, the anomalous warming does not  
680 necessarily increase deep convection since this oceanic region is already over the SST  
681 threshold for deep convection. In addition, the atmospheric teleconnections from central-  
682 eastern Pacific tend to respond strongly to a warm than cold SST anomaly as rainfall  
683 response is related to SST threshold for convection. Thus, the atmospheric teleconnections  
684 are generally stronger during El Niño than La Niña events. This may be why CMIP5 models  
685 display a stronger relationship between Niño3.4 SST variability and El Niño correlations  
686 compared to La Niña correlations.

687

688 We found statistically significant relationships between CMIP5 Niño3.4 SST variability and  
689 CMIP5 ENSO temperature and precipitation composite pattern agreement (correlations) with  
690 observations (Fig 12a). For the El Niño phase there are significant high correlations between  
691 the ONI and temperature (0.61) and precipitation (0.70) patterns. However, the relationship  
692 was much weaker for La Niña temperature (0.20) and precipitation (0.39) and was only  
693 significant for precipitation composite patterns (Fig 12b). We additionally found that there is  
694 a significant positive relationship between CMIP5 temperature and precipitation anomaly  
695 patterns for El Niño (Fig 7a) and La Niña (Fig 7b). Here again we find that the relationship is  
696 much stronger for El Niño than for La Niña, likely related to the nonlinear nature of the  
697 atmospheric response to a heating source in the equatorial Pacific as discussed previously.  
698 The reason why models that simulate well ENSO temperature patterns also have a good  
699 representation of ENSO precipitation patterns deserves further investigation. One would  
700 argue that this relationship is partially dictated by model biases: those that simulate a realistic  
701 ENSO would tend to represent atmospheric teleconnections more accurately than models  
702 with Pacific cold tongue bias. It is also intuitive to think that a realistic representation of the  
703 atmospheric mean circulation and convective parameterization schemes would affect the way  
704 ENSO teleconnections occur in climate models, as shown by previous studies (Guilyardi et  
705 al. 2004; Neale et al., 2008; Zhu et al., 2017).

706

## 707 **6. Summary and Conclusions**

708 This study provides a comprehensive evaluation of temperature and precipitation responses to  
709 ENSO variability across a range of datasets including gridded observations, reanalysis,  
710 AGCMs driven by observed SST, and coupled AOGCM simulations of the historical climate  
711 period. There is a large variety in the representation of ENSO teleconnections across this  
712 range of data products; even considering the same class of dataset (e.g., among reanalysis  
713 products) or ensemble members from the same climate model. Some climate models are able  
714 to simulate ENSO teleconnections with as high agreement as reanalysis products, while other  
715 models simulate ENSO teleconnection patterns more dissimilar to the observed ENSO  
716 responses.

717 Our study shows a clear and consistent decline in the agreement of simulated ENSO  
718 teleconnection patterns with observations for datasets with fewer observational constraints.  
719 This highlights that realistic representation of atmospheric circulation and SST variability are  
720 both key factors for realistically simulating remote relationships with ENSO. In addition, our  
721 results show that El Niño temperature and precipitation teleconnections are generally better

722 represented than La Niña patterns in reanalyses, AMIP and CMIP models. In general, models  
723 that simulate well the temperature response to ENSO also have a good representation of  
724 ENSO-related precipitation pattern, again with a better agreement for El Niño than La Niña.  
725 Overall models that simulate a larger interannual variability of central tropical Pacific SSTs  
726 tend to have a more realistic representation of El Niño teleconnections, while this relationship  
727 is weaker for La Niña. We have not found a relationship between the simulated ENSO  
728 teleconnection patterns and the horizontal resolution of the atmosphere model. The degrading  
729 of ENSO teleconnection patterns in models is thus likely be associated with factors other than  
730 model resolution, for instance model biases in the Pacific mean state and variability as well  
731 as atmosphere background circulation and convective parameterizations.  
732 Accurate simulation of ENSO teleconnections is important to enable more reliable seasonal  
733 to inter-annual climate predictions, as well as long-term future climate projections. The  
734 Pacific mean state is projected to change and the frequency of extreme ENSO events (both El  
735 Niño and La Niña) is expected to increase under greenhouse warming (Cai et al., 2014;  
736 2015a; 2015b). Therefore, understanding the relationships between ENSO and regional  
737 climate conditions becomes even more important in a future with anthropogenic climate  
738 warming. Furthermore, ENSO-driven atmospheric teleconnections are also expected to  
739 change in a warming climate (Yeh et al., 2018; Power and Delage, 2018; Perry et al., 2019),  
740 and correctly capturing these changes can be another challenge for the climate models.

741

742

#### 743 **Acknowledgments:**

744 This study was supported by funding from the Australian Research Council Centre for  
745 Climate Extremes and Climate Change Research Centre, University of New South Wales,  
746 Sydney, Australia. This project was undertaken with the assistance of resources and services  
747 from the National Computational Infrastructure (NCI), which is supported by the Australian  
748 Government. AST is supported by the Australian Research Council (FT160100465). We  
749 thank the reviewers for their constructive comments and suggestions that contributed to the  
750 improvement of this study.

751

752 **References:**

- 753 Adler, R.F., Huffman, G.J., Chang, A., Ferraro, R., Xie, P., Janowiak, J., Rudolf, B., Schneider, U.,  
754 Curtis, S., Bolvin, D., Gruber, A., Susskind, J. and Arkin, P. (2003). The Version 2 Global  
755 Precipitation Climatology Project (GPCP) Monthly Precipitation Analysis (1979-Present). *J.*  
756 *Hydrometeor.*, 4, pp.1147-1167.
- 757 Andreoli, R. V. and Kayano, M. T. (2005). ENSO-related Rainfall Anomalies in South America and  
758 Associated Circulation Features during Warm and Cold Pacific Decadal Oscillation Regimes.  
759 *International Journal of Climatology*, 25(15), pp. 2017–30.
- 760 Ashok, K., Guan, Z. and Yamagata, T., (2001). Impact of the Indian Ocean Dipole on the  
761 Relationship between the Indian Monsoon Rainfall and ENSO. *Geophysical Research Letters*, 28(23),  
762 pp.4499–4502.
- 763 Ashok, K., Behera, S., Rao, S., Weng, H. and Yamagata, T. (2007). El Niño Modoki and its possible  
764 teleconnection. *Journal of Geophysical Research*, 112, C11007.
- 765 Ashok, K., Nagaraju, C., Sen Gupta, A., and Pai, D. S. (2014). Decadal Changes in the Relationship  
766 between the Indian and Australian Summer Monsoons. *Climate Dynamics*, 42 (3), pp.1043–52.
- 767 Bosilovich, M., Chen, J., Robertson, F. and Adler, R. (2008). Evaluation of Global Precipitation in  
768 Reanalyses. *J. Appl. Meteor. Climatol.*, 47(9), pp. 2279-2299.
- 769 Burgers, G. and Stephenson, D. (1999). The “normality” of El Niño. *Geophysical Research Letters*,  
770 26(8), pp.1027-1030.
- 771 Cai, W., Borlace, S., Lengaigne, M., van Rensch, P., Collins, M., Vecchi, G., Timmermann, A.,  
772 Santoso, A., McPhaden, M., Wu, L., England, M., Wang, G., Guilyardi, E. and Jin, F. (2014).  
773 Increasing frequency of extreme El Niño events due to greenhouse warming. *Nature Climate Change*,  
774 4(2), pp.111-116.
- 775 Cai, W., Santoso, A., Wang, G., Yeh, S., An, S., Cobb, K., Collins, M., Guilyardi, E., Jin, F., Kug, J.,  
776 Lengaigne, M., McPhaden, M., Takahashi, K., Timmermann, A., Vecchi, G., Watanabe, M. and Wu,  
777 L. (2015a). ENSO and greenhouse warming. *Nature Climate Change*, 5(9), pp.849-859.
- 778 Cai, W., Wang, G., Santoso, A., McPhaden, M., Wu, L., Jin, F., Timmermann, A., Collins, M.,  
779 Vecchi, G., Lengaigne, M., England, M., Dommenget, D., Takahashi, K. and Guilyardi, E. (2015b).  
780 Increased frequency of extreme La Niña events under greenhouse warming. *Nature Climate Change*,  
781 5(2), pp.132-137.
- 782 Cai, W., Wu, L., Lengaigne, M., Li, T., McGregor, S., Kug, J.-S., Yu, J.-Y., et al. (2019). Pantropical  
783 Climate Interactions. *Science* 363, 6430, eaav4236. <https://doi.org/10.1126/science.aav4236>.
- 784 Capotondi, A., Wittenberg, A., Newman, M., Di Lorenzo, E., Yu, J., Braconnot, P., Cole, J., Dewitte,  
785 B., Giese, B., Guilyardi, E., Jin, F., Karnauskas, K., Kirtman, B., Lee, T., Schneider, N., Xue, Y. and

- 786 Yeh, S. (2015). Understanding ENSO Diversity. *Bulletin of the American Meteorological Society*,  
787 96(6), pp.921-938.
- 788 Chan, J. C. L. and Zhou, W. (2005). PDO, ENSO and the Early Summer Monsoon Rainfall over  
789 South China. *Geophysical Research Letters*, 32(8), L08810.
- 790 Copernicus Climate Change Service (C3S) (2017): ERA5: Fifth generation of ECMWF atmospheric  
791 reanalyses of the global climate. Copernicus Climate Change Service Climate Data Store (CDS),  
792 <https://cds.climate.copernicus.eu/cdsapp#!/home>
- 793 Dee, D.P. et al., 2011. The ERA-Interim reanalysis: Configuration and performance of the data  
794 assimilation system. *Quarterly Journal of the Royal Meteorological Society*, 137(656), pp.553–597.
- 795 Dieppois, B., Rouault, M. and New, M. (2015). The impact of ENSO on Southern African rainfall in  
796 CMIP5 ocean atmosphere coupled climate models. *Climate Dynamics*, 45(9-10), pp. 2425-2442.
- 797 Ecmwf.int. (2017). *Records tumble as El Niño peaks | ECMWF*. [Accessed 24 Apr. 2017]  
798 <<http://www.ecmwf.int/en/about/media-centre/news/2015/records-tumble-el-nino-peaks>>.
- 799 Frauen, C. and Dommenges, D. (2010). El Niño and La Niña amplitude asymmetry caused by  
800 atmospheric feedbacks. *Geophysical Research Letters*, 37(18).
- 801 Frauen, C., Dommenges, D., Tyrrell, N. and Rezný, M. (2014). Analysis of the Non-Linearity of El  
802 Niño Southern Oscillation Teleconnections. *Journal of Climate*, 27, 6225-6244.
- 803 Gallant, A. and Karoly, D. (2009). Atypical influence of the 2007 La Niña on rainfall and temperature  
804 in southeastern Australia. *Geophys. Res. Lett.*, 36(14).
- 805 Guilyardi, E., Gualdi, S., Slingo, J., Navarra, A., Delecluse, P., Cole, J., Madec, G., Roberts, M.,  
806 Latif, M., and Terray, L. (2004). Representing El Niño in Coupled Ocean–Atmosphere GCMs: The  
807 Dominant Role of the Atmospheric Component. *Journal of Climate*, 17, pp. 4623–29.
- 808 Harrison, D. and Vecchi, G. (1999). On the termination of El Niño. *Geophysical Research Letters*,  
809 26(11), pp.1593-1596.
- 810 Hersbach, H., Peubey, C., Simmons, A., Berrisford, P., Poli, P. and Dee, D. (2015). ERA-20CM: a  
811 twentieth-century atmospheric model ensemble. *Quarterly Journal of the Royal Meteorological  
812 Society*, 141(691), pp.2350-2375.
- 813 Hill, K. J., Taschetto, A. S. and England, M. H. (2011). Sensitivity of South American Summer  
814 Rainfall to Tropical Pacific Ocean SST Anomalies. *Geophysical Research Letters* 38(1), L01701.
- 815 Hoerling, M.P., Kumar, A., and Zhong, M. (1997). El Niño, La Niña, and the Nonlinearity of Their  
816 Teleconnections. *J. Climate*, 10, pp.1769–1786.
- 817 Huang, B., Banzon, V., Freeman, E., Lawrimore, J., Liu, W., Peterson, T., Smith, T., Thorne, P.,

- 818 Woodruff, S. and Zhang, H. (2015). Extended Reconstructed Sea Surface Temperature Version 4  
819 (ERSST.v4). Part I: Upgrades and Intercomparisons. *Journal of Climate*, 28(3), pp.911-930.
- 820 Jones, P.W., (1999). First- and Second-Order Conservative Remapping Schemes for Grids in  
821 Spherical Coordinates. *Monthly Weather Review*, 127(9), pp.2204–2210.
- 822 Jourdain, N., Gupta, A., Taschetto, A., Ummenhofer, C., Moise, A. and Ashok, K. (2013). The Indo-  
823 Australian monsoon and its relationship to ENSO and IOD in reanalysis data and the CMIP3/CMIP5  
824 simulations. *Climate Dynamics*, 41(11-12), pp.3073-3102.
- 825 Kanamitsu, M. et al., (2002). Ncep--doe amip-ii reanalysis (r-2). *Bulletin of the American*  
826 *Meteorological Society*, 83(11), pp.1631–1643.
- 827 Kidston, J. and Gerber, E. (2010). Intermodel variability of the poleward shift of the austral jet stream  
828 in the CMIP3 integrations linked to biases in 20th century climatology. *Geophysical Research Letters*,  
829 37(9).
- 830 Kim, J.-W., Yeh, S.-W., and Chang, E.-C. (2014) Combined Effect of El Niño-Southern Oscillation  
831 and Pacific Decadal Oscillation on the East Asian Winter Monsoon. *Climate Dynamics*, 42(3),  
832 pp.957–71.
- 833 King, A., Alexander, L. and Donat, M. (2013). Asymmetry in the response of eastern Australia  
834 extreme rainfall to low-frequency Pacific variability. *Geophysical Research Letters*, 40(10), pp.2271-  
835 2277.
- 836 King, A., Donat, M., Alexander, L. and Karoly, D. (2015). The ENSO-Australian rainfall  
837 teleconnection in reanalysis and CMIP5. *Climate Dynamics*, 44(9-10), pp.2623-2635.
- 838 Kobayashi, S., Ota, Y., Harada, Y., Ebata, A., Moriya, M., Onoda, H., Onogi, K., et al. (2015). The  
839 JRA-55 Reanalysis: General Specifications and Basic Characteristics. *Journal of the Meteorological*  
840 *Society of Japan*, 93(1), pp.5–48.
- 841 Langenbrunner, B. and Neelin, J. (2013). Analyzing ENSO Teleconnections in CMIP Models as a  
842 Measure of Model Fidelity in Simulating Precipitation. *Journal of Climate*, 26(13), pp.4431-4446.
- 843 Larkin, N. and Harrison, D. (2002). ENSO Warm (El Niño) and Cold (La Niña) Event Life Cycles:  
844 Ocean Surface Anomaly Patterns, Their Symmetries, Asymmetries, and Implications. *Journal of*  
845 *Climate*, 15(10), pp.1118-1140.
- 846 Lenssen, N., G. Schmidt, J. Hansen, M. Menne, A. Persin, R. Ruedy, and D. Zyss. (2019).  
847 Improvements in the GISTEMP uncertainty model. *J. Geophys. Res. Atmos.*, 124(12), pp.6307-6326.
- 848 Lim, E. and Hendon, H. (2015). Understanding and predicting the strong Southern Annular Mode and  
849 its impact on the record wet east Australian spring 2010. *Climate Dynamics*, 44(9-10), pp.2807-2824.
- 850 McPhaden, M., Zebiak, S. and Glantz, M. (2006). ENSO as an Integrating Concept in Earth Science.

- 851 *Science*, 314(5806), pp.1740-1745.
- 852 Morice, C. P., Kennedy, J. J., Rayner, N. A. and Jones, P. D. (2012). Quantifying uncertainties in  
853 global and regional temperature change using an ensemble of observational estimates: The  
854 HadCRUT4 dataset, *J. Geophys. Res.-Atmos.*, 117, D8, doi:10.1029/2011JD017187.
- 855 Neale, R. B., Richter, J. H., and Jochum, M. (2008). The Impact of Convection on ENSO: From a  
856 Delayed Oscillator to a Series of Events. *Journal of Climate*, 21(22), pp.5904–5924.
- 857 Nicholson, S. and Kim, J. (1997). The Relationship of the El Niño-Southern Oscillation to African  
858 Rainfall. *International Journal of Climatology*, 17(2), pp.117-135.
- 859 NOAA/CPC. (2016). Climate Prediction Centre - Monitoring & Data: ENSO Impacts on the U.S.  
860 [online], Accessed 10 Sep. 2016  
861 <[http://www.cpc.ncep.noaa.gov/products/analysis\\_monitoring/ensostuff/ensoyears.shtml](http://www.cpc.ncep.noaa.gov/products/analysis_monitoring/ensostuff/ensoyears.shtml)>
- 862 NOAA/NCEI. (2016). National Centers for Environmental Information - Equatorial Pacific Sea  
863 Surface Temperatures, digital image. [online] Accessed 16 Sep. 2016  
864 <<https://www.ncdc.noaa.gov/teleconnections/enso/indicators/sst.php>>
- 865 Nobre, P., and Shukla, J. (1996). Variations of Sea Surface Temperature, Wind Stress, and Rainfall  
866 over the Tropical Atlantic and South America. *Journal of Climate*, 9, pp.2464–2479.
- 867 Perry, S. J., McGregor, S., Sen Gupta, A., England, M. H., Maher, N. (2019). Projected Late 21st  
868 Century Changes to the Regional Impacts of the El Niño-Southern Oscillation. *Climate Dynamics*,  
869 <https://doi.org/10.1007/s00382-019-05006-6>.
- 870 Poli, P., Hersbach, H., Dee, D., Berrisford, P., Simmons, A., Vitart, F., Laloyaux, P., Tan, D., Peubey,  
871 C., Thépaut, J., Trémolet, Y., Hólm, E., Bonavita, M., Isaksen, L. and Fisher, M. (2016). ERA-20C:  
872 An Atmospheric Reanalysis of the Twentieth Century. *Journal of Climate*, 29(11), pp.4083-4097.
- 873 Power, S. B., and Delage, F. P. D. (2018). El Niño–Southern Oscillation and Associated Climatic  
874 Conditions around the World during the Latter Half of the Twenty-First Century. *Journal of Climate*,  
875 31(15), pp. 6189–6207.
- 876 Power, S., Casey, T., Folland, C., Colman, A. and Mehta, V. (1999). Inter-decadal modulation of the  
877 impact of ENSO on Australia. *Climate Dynamics*, 15(5), pp.319-324.
- 878 Rodrigues, R. R., Haarsma, R. J., Campos, E. J. D. and Ambrizzi, T. 2011. The Impacts of Inter-El  
879 Niño Variability on the Tropical Atlantic and Northeast Brazil Climate. *Journal of Climate* 24(13),  
880 3402–22.
- 881 Ropelewski, C. and Halpert, M. (1987). Global and Regional Scale Precipitation Patterns Associated  
882 with the El Niño/Southern Oscillation. *Monthly Weather Review*, 115(8), pp.1606-1626.

- 883 Scaife, A., Woollings, T., Knight, J., Martin, G. and Hinton, T. (2010). Atmospheric Blocking and  
884 Mean Biases in Climate Models. *Journal of Climate*, 23(23), pp.6143-6152.
- 885 Schneider, U., Becker, A., Finger, P., Meyer-Christoffer, A., Rudolf, B., Ziese, M. (2011). GPCP Full  
886 Data Reanalysis Version 6.0 at 1.0°: Monthly Land-Surface Precipitation from Rain-Gauges built on  
887 GTS-based and Historic Data. DOI: 10.5676/DWD\_GPCC/FD\_M\_V7\_100.
- 888 Taschetto, A. S., Ummenhofer, C. C. Sen Gupta, A. and England, M. H. (2009). Effect of Anomalous  
889 Warming in the Central Pacific on the Australian Monsoon. *Geophysical Research Letters*, 36,  
890 L12704.
- 891 Taschetto, A. S., Sen Gupta, A., Hendon, H., Ummenhofer, C. C. and England, M. H. (2011). The  
892 Contribution of Indian Ocean Sea Surface Temperature Anomalies on Australian Summer Rainfall  
893 during El Niño Events. *Journal of Climate*, 24(14), pp.3734-3747.
- 894 Taschetto, A. S., Sen Gupta, A., Jourdain, N., Santoso, A., Ummenhofer, C. C. and England, M. H.  
895 (2014). Cold Tongue and Warm Pool ENSO Events in CMIP5: Mean State and Future Projections.  
896 *Journal of Climate*, 27(8), pp.2861-2885.
- 897 Taylor, K., Stouffer, R. and Meehl, G. (2012). An Overview of CMIP5 and the Experiment Design.  
898 *Bull. Amer. Meteor. Soc.*, 93(4), pp.485-498.
- 899 Tedeschi, R., Cavalcanti, I. and Grimm, A. (2013). Influences of two types of ENSO on South  
900 American precipitation. *International Journal of Climatology*, 33(6), pp.1382-1400.
- 901 Trenberth, K. E., Branstator, G. W., Karoly, D., Kumar, A., Lau, N.-C., and Ropelewski, C. (1998).  
902 Progress during TOGA in Understanding and Modeling Global Teleconnections Associated with  
903 Tropical Sea Surface Temperatures. *Journal of Geophysical Research*, 103(C7), pp.14291–324.
- 904 Trenberth, K. E., and Stepaniak, D. P. (2001). Indices of El Niño Evolution. *Journal of Climate*,  
905 14(8), pp.1697–1701.
- 906 Ummenhofer, C., England, M., McIntosh, P., Meyers, G., Pook, M., Risbey, J., Sen Gupta, A. and  
907 Taschetto, A. S. (2009). What causes southeast Australia's worst droughts? *Geophysical Research*  
908 *Letters*, 36(4), pp.1-6.
- 909 Ummenhofer, C., Sen Gupta, A., Li, Y., Taschetto, A. S., and England, M. (2011). Multi-decadal  
910 modulation of the El Niño–Indian monsoon relationship by Indian Ocean variability. *Environmental*  
911 *Research Letters*, 6(3), p.034006.
- 912 Weare, B. (2012). El Niño teleconnections in CMIP5 models. *Climate Dynamics*, 41(7-8), pp. 2165-  
913 2177.
- 914 Weng, H., Ashok, K., Behera, S. K., Rao, S. A., and Yamagata, T. (2007). Impacts of Recent El Niño  
915 Modoki on Dry/Wet Conditions in the Pacific Rim during Boreal Summer. *Climate Dynamics*, 29(2–  
916 3), pp.113–129.

- 917 Wilks, D.S. (1995). *Statistical Methods in the Atmospheric Sciences: An Introduction*. Academic  
918 Press, 467 pp.
- 919 Wittenberg, A. T. (2009) Are Historical Records Sufficient to Constrain ENSO Simulations?  
920 *Geophysical Research Letters*, 36(12), L12702. <https://doi.org/10.1029/2009GL038710>.
- 921 Xie, P., and Arkin, P. A. (1997). Global precipitation: A 17-year monthly analysis based on gauge  
922 observations, satellite estimates, and numerical model outputs. *Bull. Amer. Meteor. Soc.*, 78, 2539 -  
923 2558.
- 924 Yang, X. and DelSole, T. (2012). Systematic Comparison of ENSO Teleconnection Patterns between  
925 Models and Observations. *Journal of Climate*, 25(2), pp.425-446.
- 926 Yeh, S., Cai, W., Min, S., McPhaden, M., Dommenges, D., Dewitte, B., Collins, M., Ashok, K., An,  
927 S., Yim, B. and Kug, J. (2018). ENSO Atmospheric Teleconnections and Their Response to  
928 Greenhouse Gas Forcing. *Reviews of Geophysics*, 56(1), pp.185-206.
- 929 Yoon, J. and Yeh, S.-W. (2010) Influence of the Pacific Decadal Oscillation on the Relationship  
930 between El Niño and the Northeast Asian Summer Monsoon. *Journal of Climate* 23(17), pp. 4525–37.
- 931 Yulaeva, E., and Wallace, J. M. (1994). The Signature of ENSO in Global Temperature and  
932 Precipitation Fields Derived from the Microwave Sounding Unit. *Journal of Climate*, 7(11), pp.  
933 1719–36.
- 934 Zhu, J., Kumar, A., Wang, W., Hu, Z.-Z., Huang, B., and Balmaseda, A. A. (2017). Importance of  
935 Convective Parameterization in ENSO Predictions. *Geophys. Res. Lett.*, 44(12), pp. 6334–42.
- 936 Zou, Y., Yu, J., Lee, T., Lu, M. and Kim, S. (2014). CMIP5 model simulations of the impacts of the  
937 two types of El Niño on the U.S. winter temperature. *Journal of Geophysical Research: Atmospheres*,  
938 119(6), pp.307.
- 939 Zwiers, F.W. and von Storch, H. (1995). [Taking Serial Correlation into Account in Tests of the](#)  
940 [Mean](#). *J. Climate*, 8, pp.336–351.

941 **Table 1:** CMIP5 models used in this study; the providing institutes; the longitude-latitude  
942 grid box resolutions of the atmosphere component; number of model realisations used to  
943 calculate mean temperature and total precipitation. Models with (\*) additionally provide  
944 AMIP runs.

	<b>Model</b>	<b>Institute, Country</b>	<b>Atmosphere resolution</b>	<b>#Runs</b>
1	ACCESS1-0 *	Australian Commonwealth Scientific and Industrial Research Organisation (CSIRO) Bureau of Meteorology (BOM), Australia	1.875° x 1.25°	2
2	ACCESS1-3			3
3	BCC-CSM1-1 *	Beijing Climate Centre (BCC) China and Meteorological Administration, China	2.8° x 2.8°	3
4	BCC-CSM1-1-M *			3
5	BNU-ESM	Beijing Normal University, China	2.8° x 2.8°	1
6	CanESM2 *	Canadian Centre for Climate Modelling and Analysis (CCCMA), Canada	2.8° x 2.8°	5
7	CCSM4 *	National Centre for Atmospheric Research (NCAR), USA	1.25° x 0.94°	7
8	CESM1-BGC			1
9	CESM1-CAM5			3
10	CESM1-FASTCHEM *		3	
11	CESM1-WACCM		2.5° x 1.9°	1
12	CMCC-CESM	Centro Euro-Mediterraneo per i Cambiamenti Climatici (CMCC), Italy	3.75° x 3.75°	1
13	CMCC-CM *		0.75° x 0.75°	1
14	CMCC-CMS *		1.875° x 1.875°	1
15	CNRM-CM5 *	Centre National de Recherches Meteorologiques (CNRM) and Centre European de Recherches et de Formation Avancee en Calcul Scientifique (CERFACS), France	1.4° x 1.4°	10
16	CNRM-CM5-2			1
17	CSIRO-Mk3-6-0 *	CSIRO and Queensland Climate Change Centre of Excellence (QCCCE), Australia	1.875° 1.875°	10
18	CSIRO-Mk3L-1-2		5.6° x 3.2°	3
19	EC-EARTH *	Royal Netherlands Meteorological Institute, The Netherlands	1.125° x 1.125°	6
20	FIO-ESM	The First Institution of Oceanography (FIO), China	2.8° x 2.8°	3
21	GFDL-CM2p1	NOAA Geophysical Fluid Dynamics Laboratory (GFDL), USA	2.5° x 2.0°	10
22	GFDL-CM3 *			5
23	GFDL-ESM2G *			1
24	GFDL-ESM2M *			1
25	GISS-E2-H			17
26	GISS-E2-R *	National Aeronautics and Space Administration (NASA) and Godard Institute for Space Studies (GISS), USA		25
27	GISS-E2-R-CC			1
28	HadCM3 *	Met Office Hadley Centre (MOHC), UK	3.75° x 2.5°	10
29	HadGEM2-ES *		1.875° x 1.25°	5
30	INMCM4 *	Institute for Numerical Mathematics (INM), Russia	2.0° x 1.5°	1
31	IPSL-CM5A-LR *	Institut Pierre Simon Laplace, France	3.75 x 1.875°	6
32	IPSL-CM5A-MR *		2.5° x 1.25°	3
33	IPSL-CM5B-LR *		3.75° x 1.875°	1
34	MIRCO5 *	Atmosphere and Ocean Research Institute (AORI) and National Institute for Environmental Studies (NIES) and Japan Agency for Marine-Earth Science and Technology (JAMSTEC)	1.41° x 1.41°	5
35	MIROC-ESM *		2.81° x 2.81°	3
36	MIROC-ESM-CHEM *		1	
37	MPI-ESM-LR *	Max Planck Institute for Meteorology (MPI-M), Germany	1.875° x 1.875°	3
38	MPI-ESM-MR *			3
39	MPI-ESM-P *			2
40	MRI-CGCM3 *	Meteorological Research Institute (MRI), Japan	1.125° x 1.125°	5
41	MRI-ESM1			1
42	NorESM1-M *	Norwegian Climate Centre (NCC), Norway	2.5° x 1.875°	3
43	NorESM1-ME			1

945

946 **Table 2:** Temperature and precipitation anomaly map correlations to CRU averaged for each  
947 dataset. Correlations of El Niño (red) and La Niña (blue) of 40NS and global fields are  
948 derived from May-April ENSO year averages and peak month averages (shown in brackets).  
949 Correlations are separated for the 1945-2005 investigation period and 1979-2005 AMIP  
950 period. Note that ERA-20CM values are of the ensemble mean.  
951

	Temperature		Precipitation	
	40°N - 40°S	Global	40°N - 40°S	Global
<b>1945-2005</b>				
ERA-20C	0.78 (0.77), 0.53 (0.59)	0.83 (0.87), 0.71 (0.78)	0.73 (0.71), 0.60 (0.64)	0.66 (0.64), 0.53 (0.60)
ERA-20CM	0.63 (0.61), 0.45 (0.42)	0.54 (0.43), 0.52 (0.30)	0.66 (0.67), 0.59 (0.52)	0.55 (0.52), 0.47 (0.42)
GISS	0.83 (0.87) 0.72 (0.80)	0.91 (0.92) 0.83 (0.90)	---	---
HadCRU	0.83 (0.87) 0.75 (0.80)	0.84 (0.89) 0.80 (0.88)	---	---
GPCC	---	---	0.82 (0.77) 0.80 (0.76)	0.80 (0.76) 0.76 (0.77)
CMIP5	0.45 (0.33), 0.25 (0.24)	0.29 (0.19), 0.16 (0.13)	0.44 (0.41), 0.34 (0.25)	0.33 (0.31), 0.24 (0.19)
<b>1979-2005</b>				
ERA-20C	0.72 (0.69), 0.55 (0.46)	0.77 (0.81), 0.71 (0.72)	0.67 (0.69), 0.57 (0.55)	0.62 (0.64), 0.51 (0.52)
ERA-20CM	0.58 (0.56), 0.50 (0.39)	0.61 (0.42), 0.47 (0.26)	0.61 (0.60), 0.50 (0.32)	0.51 (0.51), 0.35 (0.23)
GPCP	---	---	0.81 (0.75) 0.77 (0.72)	0.75 (0.72) 0.74 (0.72)
CMAF	---	---	0.75 (0.76) 0.64 (0.65)	0.68 (0.70) 0.61 (0.64)
ERA5	0.84 (0.85) 0.72 (0.61)	0.87 (0.89) 0.80 (0.82)	0.63 (0.53) 0.42 (0.57)	0.55 (0.51) 0.41 (0.58)
<b>1948-2005</b>				
NCEP/NCAR	0.71 (0.66) 0.56 (0.66)	0.79 (0.80) 0.71 (0.81)	0.54 (0.54) 0.22 (0.44)	0.49 (0.51) 0.26 (0.47)
<b>1958-2005</b>				
JRA55	0.72 (0.78) 0.61 (0.72)	0.83 (0.87) 0.78 (0.84)	---	---
AMIP5	0.45 (0.46), 0.35 (0.32)	0.38 (0.32), 0.20 (0.08)	0.42 (0.40), 0.35 (0.22)	0.31 (0.30), 0.24 (0.15)
CMIP5	0.28 (0.22), 0.14 (0.16)	0.20 (0.11), 0.02 (0.00)	0.30 (0.31), 0.23 (0.17)	0.21 (0.22), 0.16 (0.11)

952

953

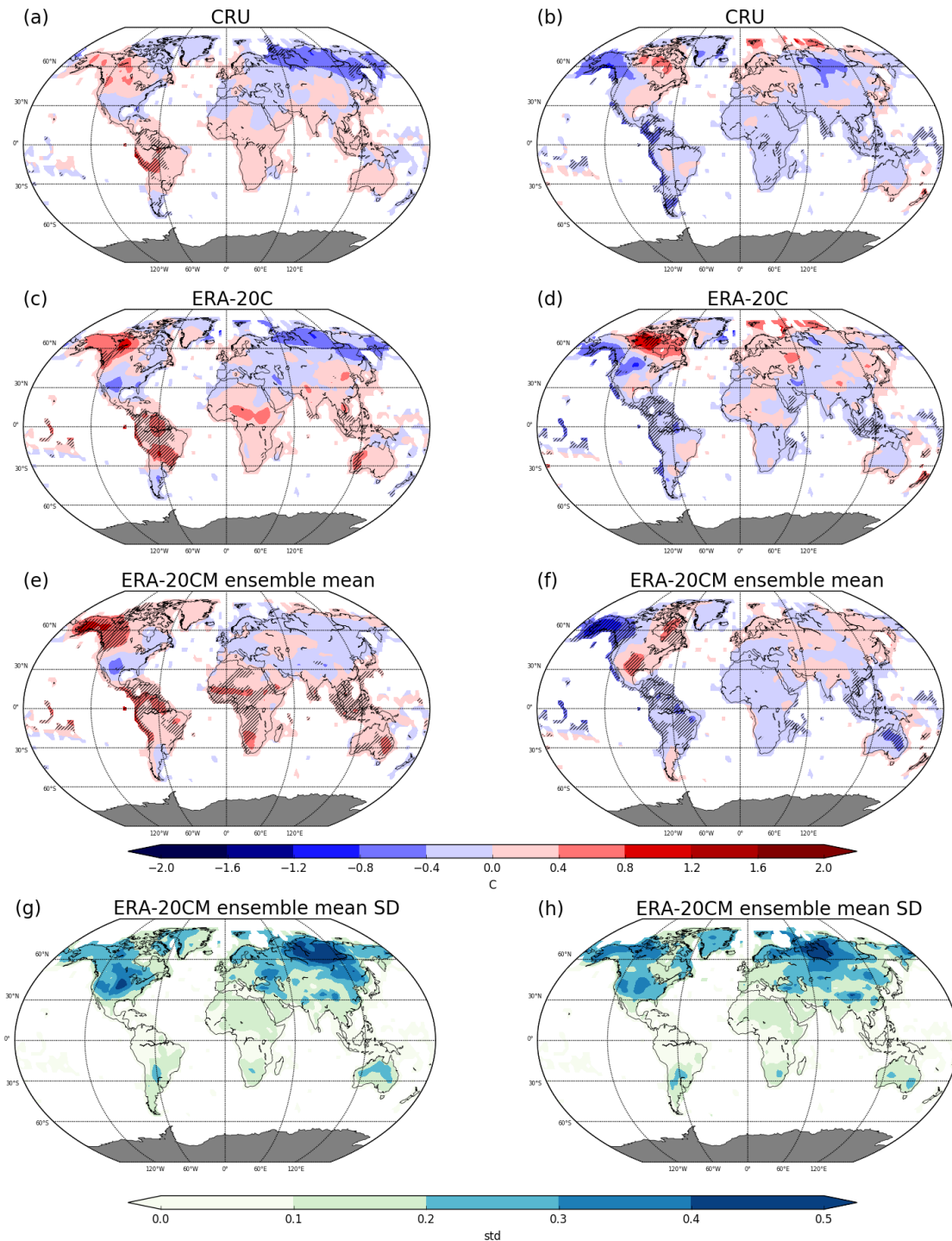
954 **Table 3:** Temperature and precipitation anomaly map correlations to ERA-20C averaged for  
 955 each dataset. Correlations of El Niño (red) and La Niña (blue) of 40NS and global fields are  
 956 derived from May-April ENSO year averages and peak month averages (shown in brackets).  
 957 Correlations are separated for the 1945-2005 investigation period and 1979-2005 AMIP  
 958 period. Note that ERA-20CM values are of the ensemble mean.  
 959

	Temperature		Precipitation	
	40°N - 40°S	Global	40°N - 40°S	Global
<b>1945-2005</b>				
ERA-20CM	0.73 (0.67), 0.60 (0.61)	0.66 (0.50), 0.57 (0.39)	0.75 (0.76), 0.61 (0.57)	0.64 (0.58), 0.48 (0.50)
CMIP5	0.49 (0.39), 0.27 (0.26)	0.34 (0.22), 0.16 (0.13)	0.48 (0.46), 0.31 (0.25)	0.38 (0.34), 0.22 (0.18)
<b>1979-2005</b>				
ERA-20CM	0.66 (0.58), 0.60 (0.51)	0.59 (0.38), 0.49 (0.31)	0.77 (0.76), 0.57 (0.47)	0.64 (0.61), 0.40 (0.36)
AMIP5	0.56 (0.51), 0.41 (0.40)	0.44 (0.33), 0.23 (0.13)	0.51 (0.50), 0.41 (0.32)	0.39 (0.37), 0.28 (0.23)
CMIP5	0.36 (0.29), 0.13 (0.18)	0.21 (0.12), 0.01 (0.01)	0.35 (0.35), 0.26 (0.25)	0.26 (0.25), 0.17 (0.17)

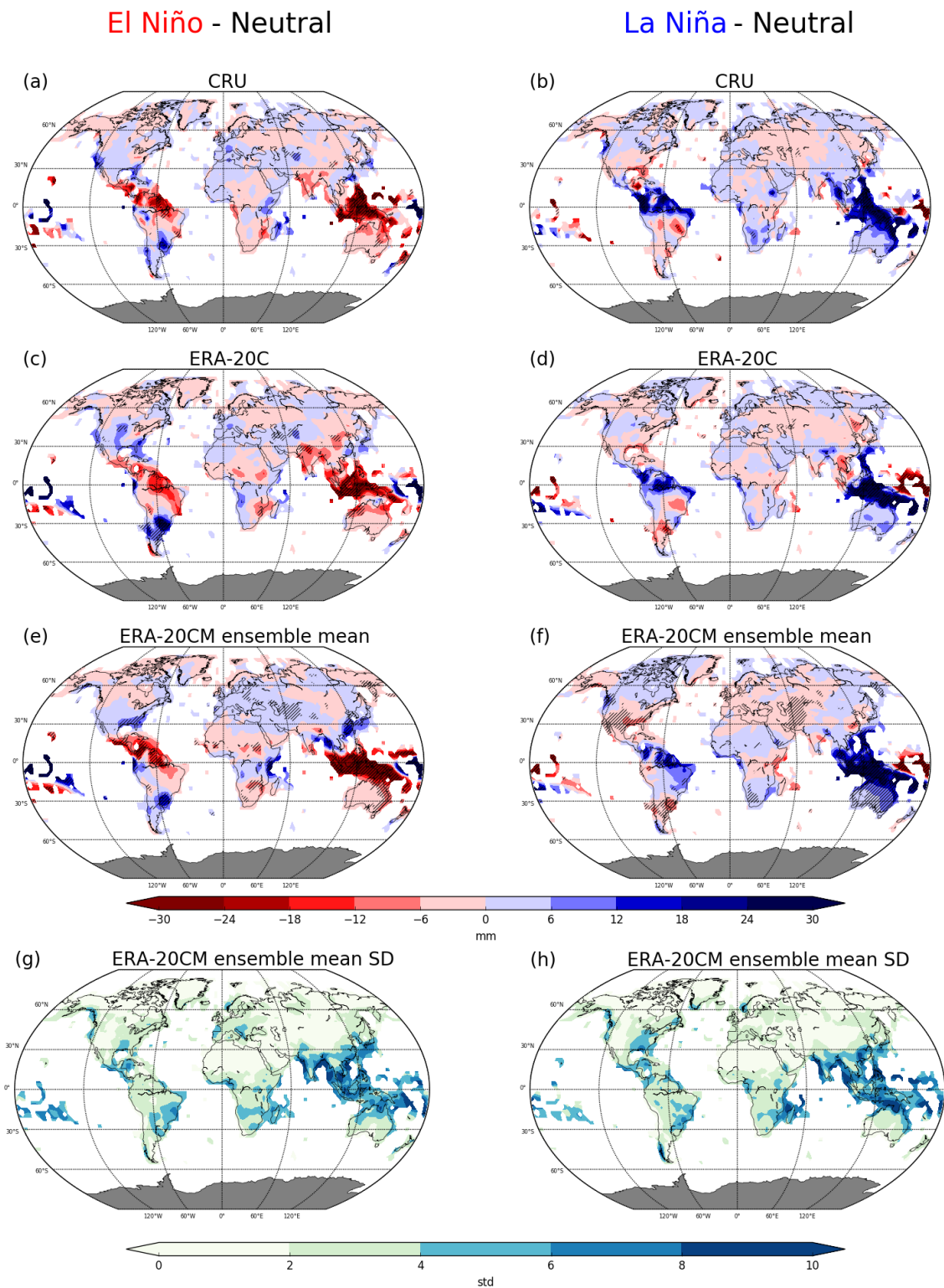
960

El Niño - Neutral

La Niña - Neutral



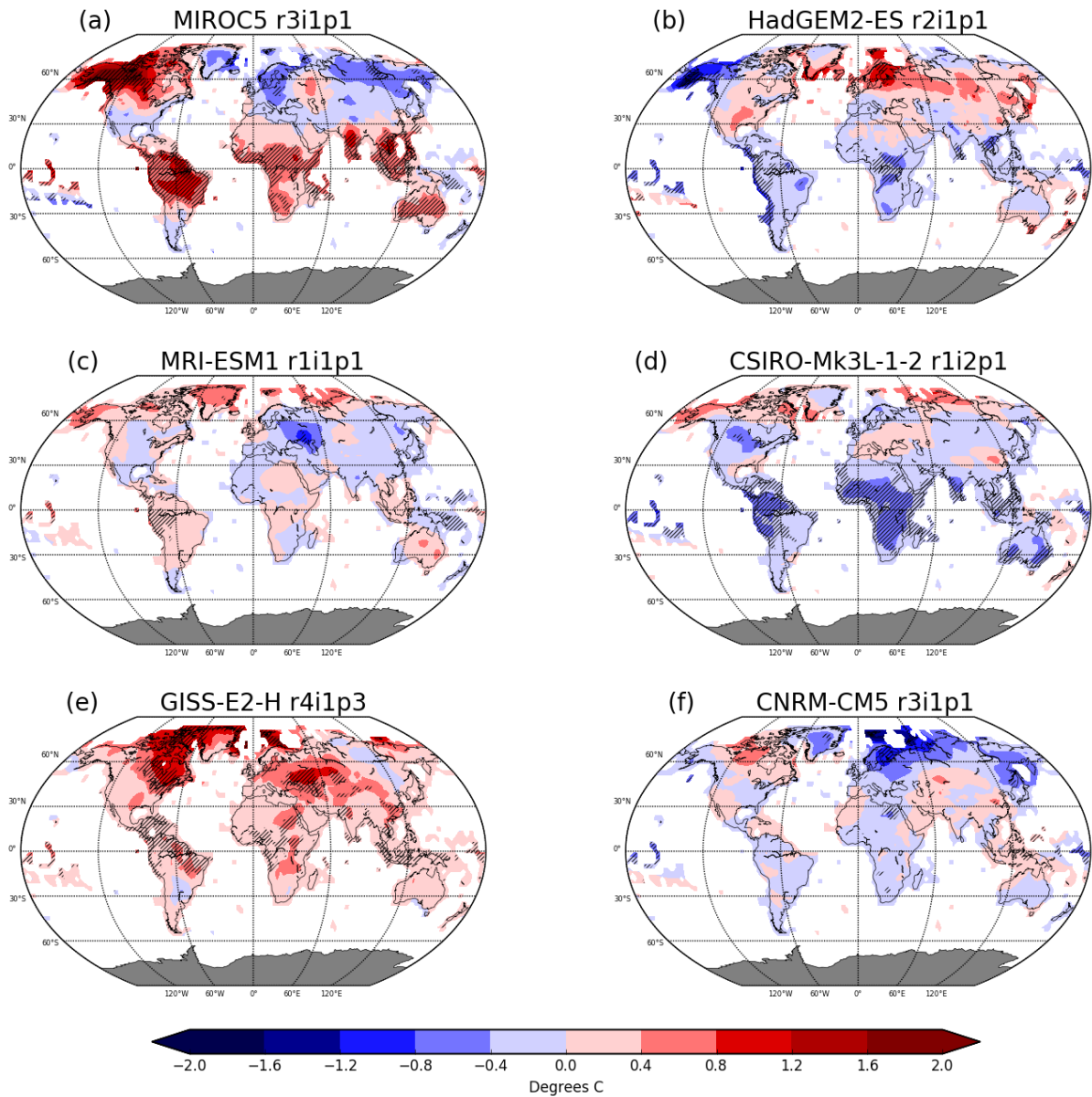
961  
 962 **Fig 1:** Composite patterns of El Niño (left) and La Niña (right) temperature anomalies  
 963 between 1945-2005, relative to the temperature in neutral ENSO conditions. The maps  
 964 display warm (red) and cool (blue) anomalies from (top) CRU, (second row) ERA-20C,  
 965 (third row) ERA-20CM ensemble mean. Hatching represents regions where anomalies are  
 966 significantly different from neutral years at the 5% level using local KS tests. The bottom  
 967 row shows the standard deviation across the ten ERA-20CM ensemble members.



968 **Fig 2:** Composite patterns of El Niño (left) and La Niña (right) precipitation anomalies  
 969 between 1945-2005, relative to precipitation in neutral ENSO conditions. The maps display  
 970 wet (blue) and dry (red) anomalies from (top) CRU, (second row) ERA-20C, (third row)  
 971 ERA-20CM ensemble mean. Hatching represents regions where anomalies are significantly  
 972 different from neutral years at the 5% level using local KS tests. The bottom row shows the  
 973 standard deviation across the ten ERA-20CM ensemble members.

## El Niño - Neutral

## La Niña - Neutral

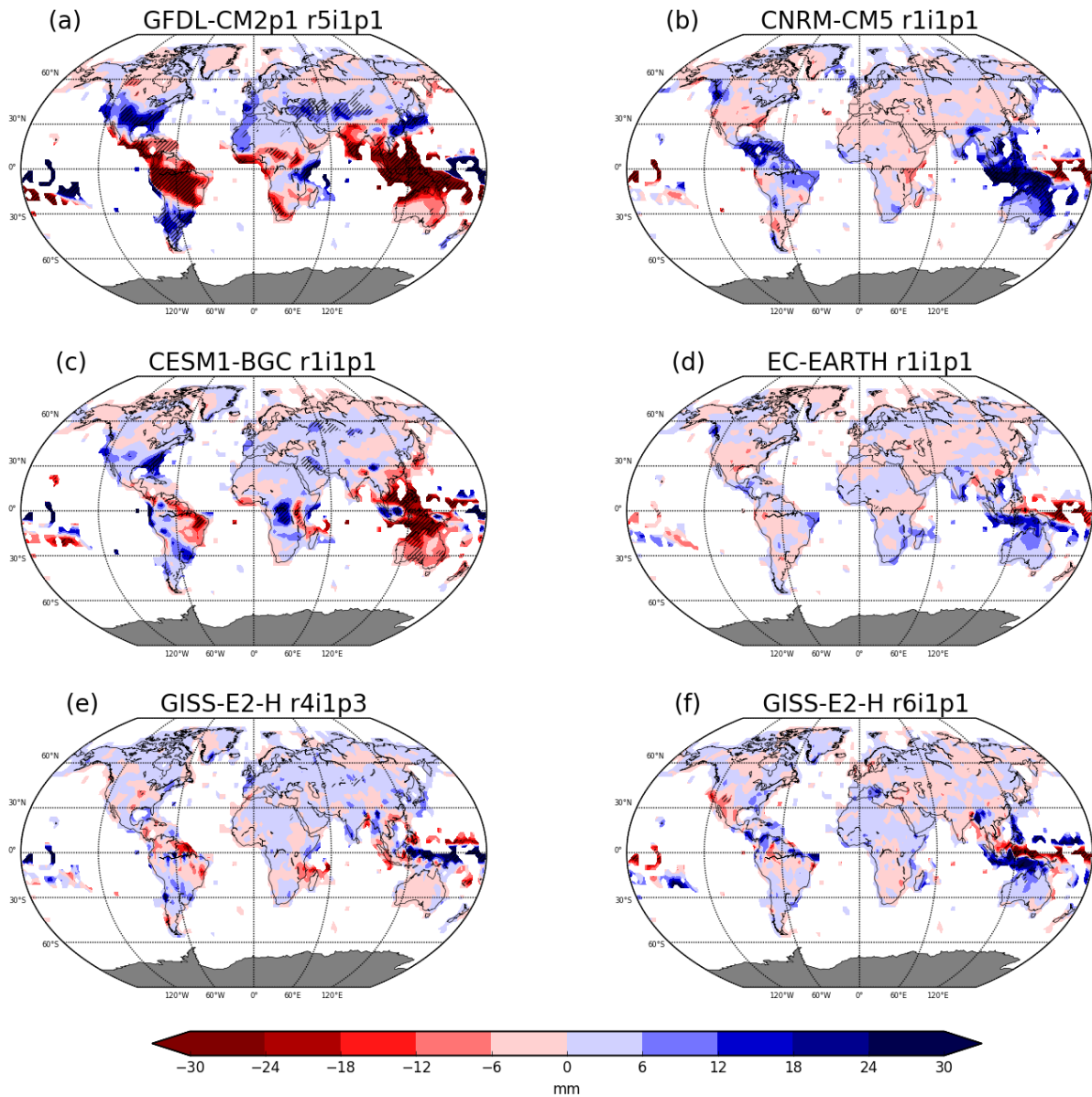


974 **Fig 3:** Composites of temperature anomalies during El Niño (left) and La Niña (right)  
975 conditions relative to neutral between 1945-2005. The maps show anomalies from selected  
976 CMIP5 models with the highest (top), median (middle) and lowest (bottom) spatial  
977 correlations to CRU. Hatching represents regions where anomalies are significantly different  
978 from neutral years at the 5% level using local KS tests.

979  
980  
981  
982  
983

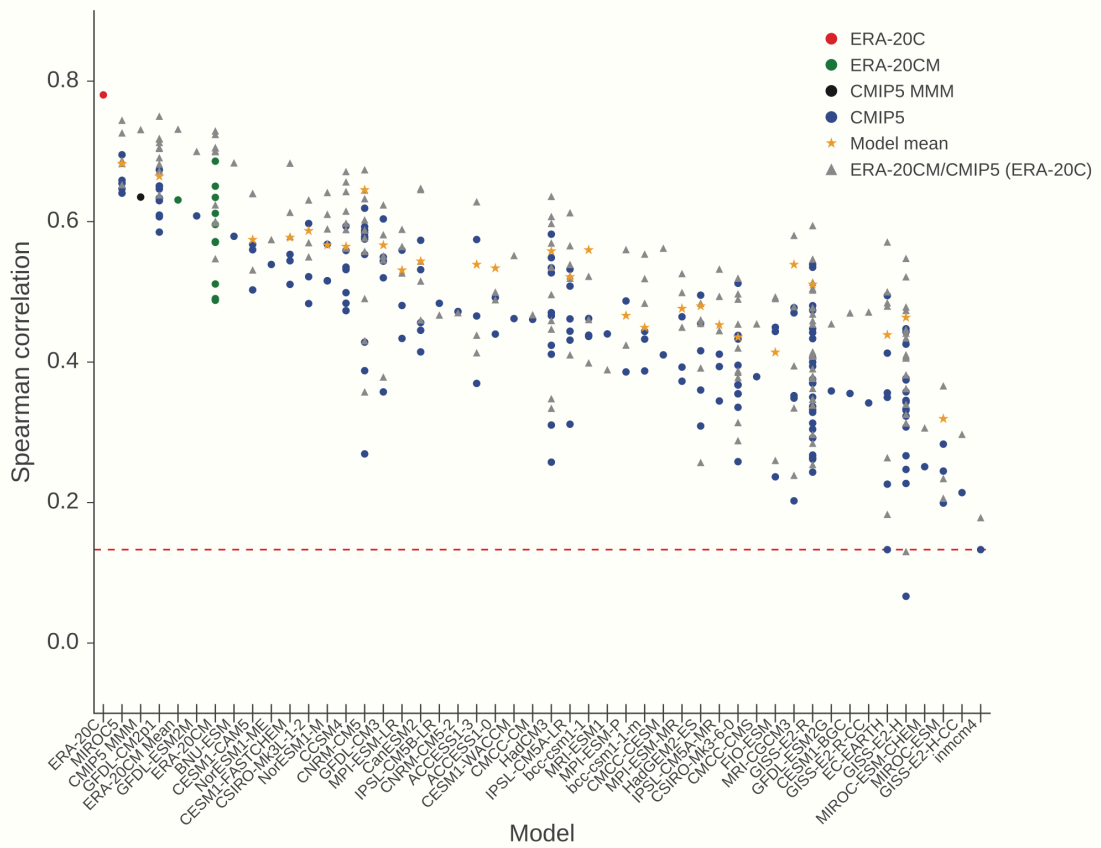
## El Niño - Neutral

## La Niña - Neutral

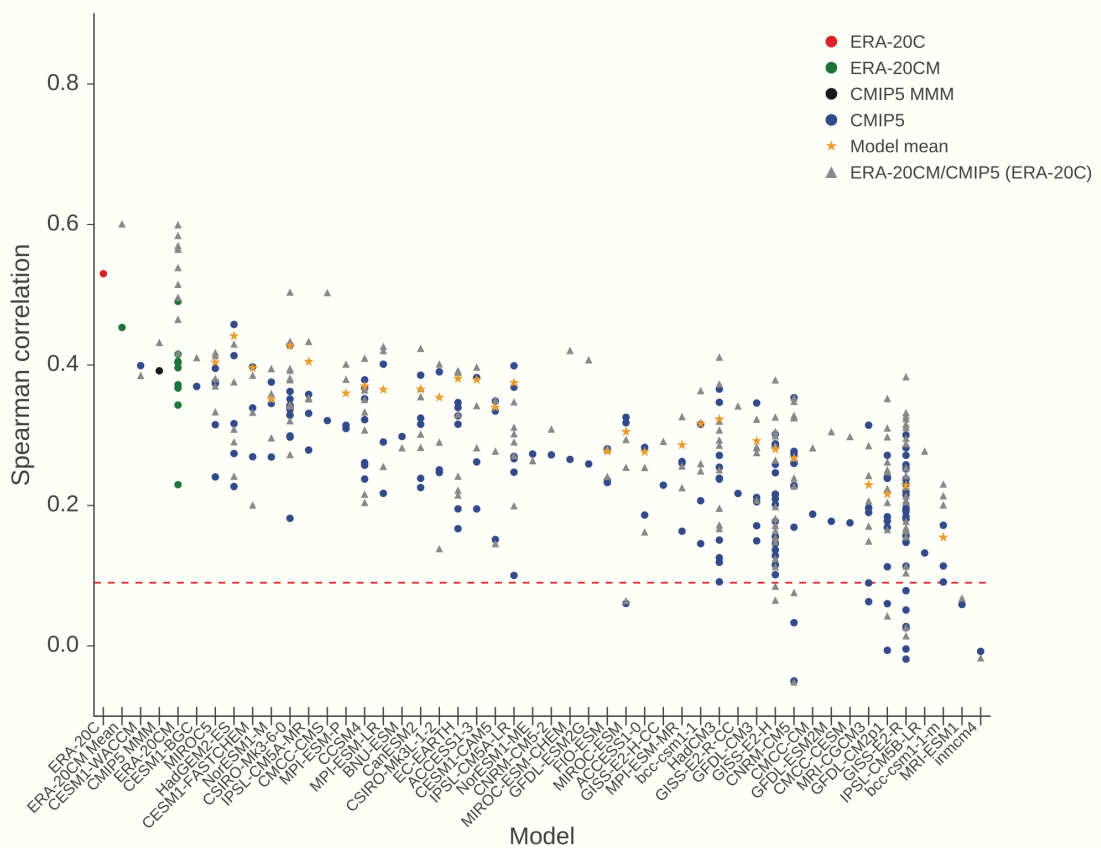


984 **Fig 4:** Composites of precipitation anomalies during El Niño (left) and La Niña (right)  
985 relative to neutral conditions between 1945-2005. The maps show anomalies from selected  
986 CMIP5 models with the highest (top), median (middle) and lowest (bottom) spatial  
987 correlations to CRU. Hatching represents regions where anomalies are significantly different  
988 from neutral years at the 5% level using local KS tests.

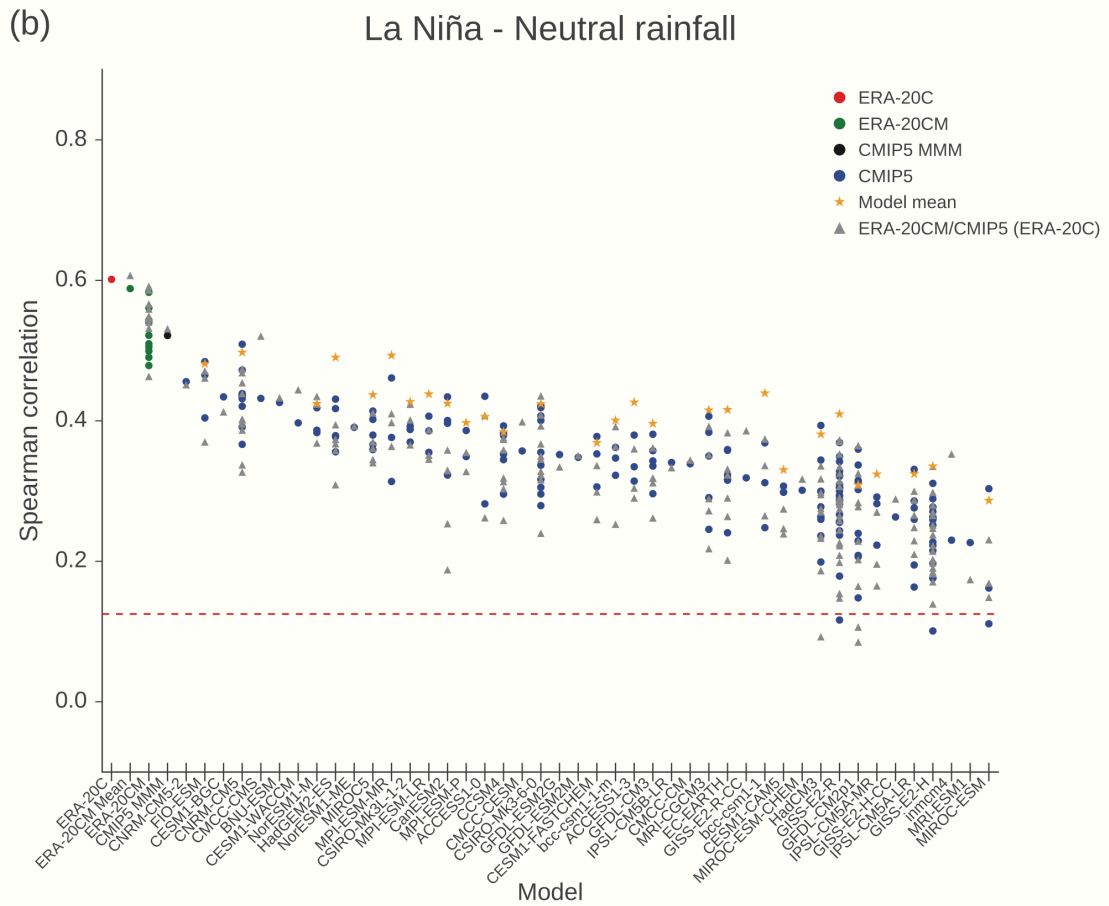
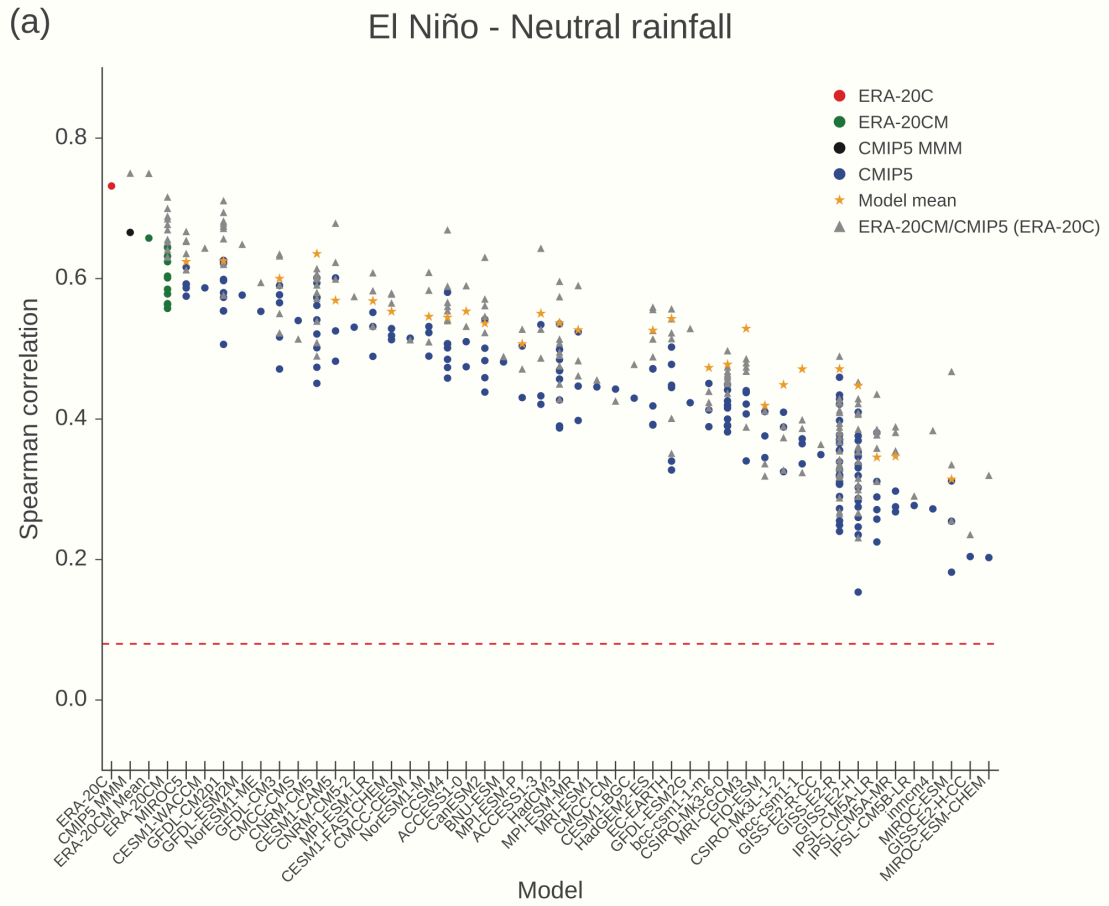
(a) El Niño - Neutral temperature



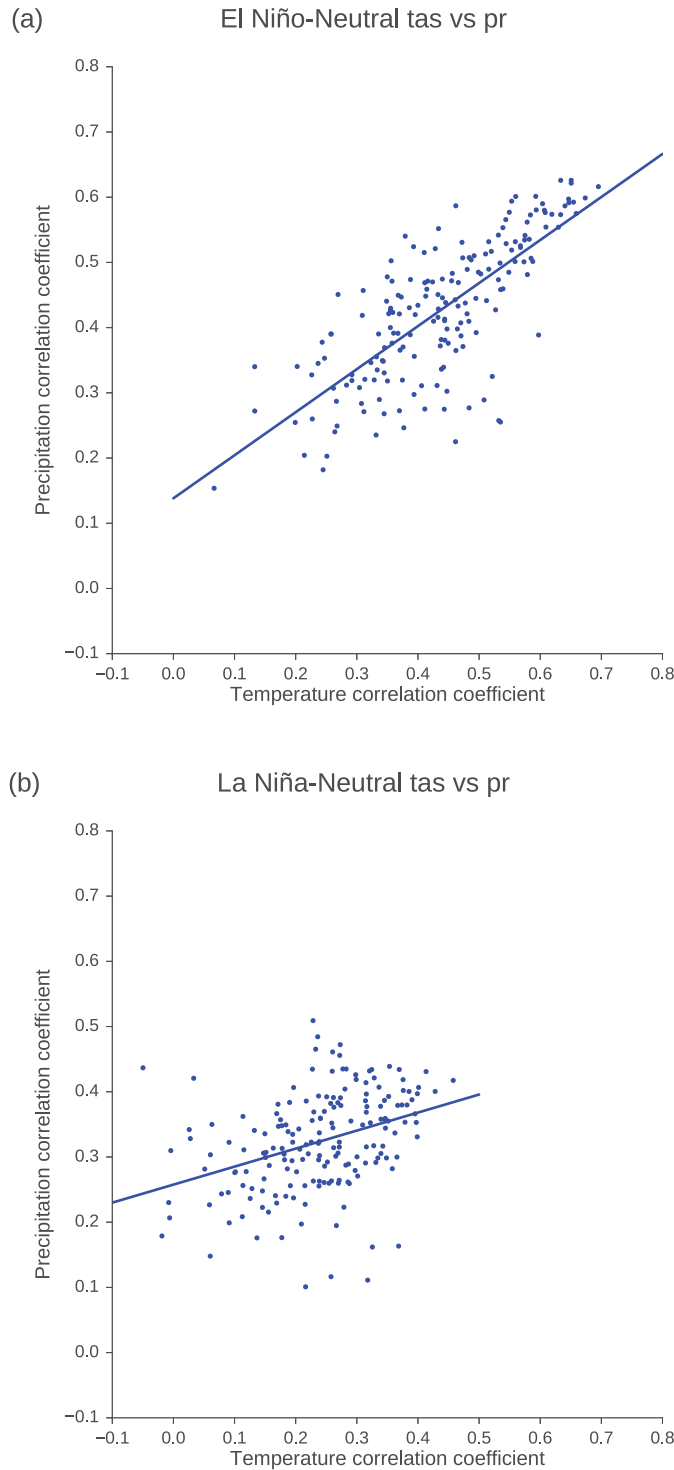
(b) La Niña - Neutral temperature



990 **Fig 5:** El Niño (a) and La Niña (b) pattern correlations of temperature anomalies between  
991 40°N - 40°S during 1945-2005 compared to CRU. CMIP5 models (blue), ERA-20CM  
992 (green) and ERA-20C (red) are ordered on the x-axis left to right by the average of their  
993 correlations. Grey triangles represent the same composite patterns correlated to ERA-20C.  
994 Individual model ensemble averages are shown by yellow stars, and the CMIP5 multi-model  
995 ensemble mean (using the individual model ensemble means from models with multiple  
996 realisations and single realisations from models providing only one simulation) by the black  
997 filled circle. The red dotted lines represent the threshold at which correlations are statistically  
998 significant at the 5% level.

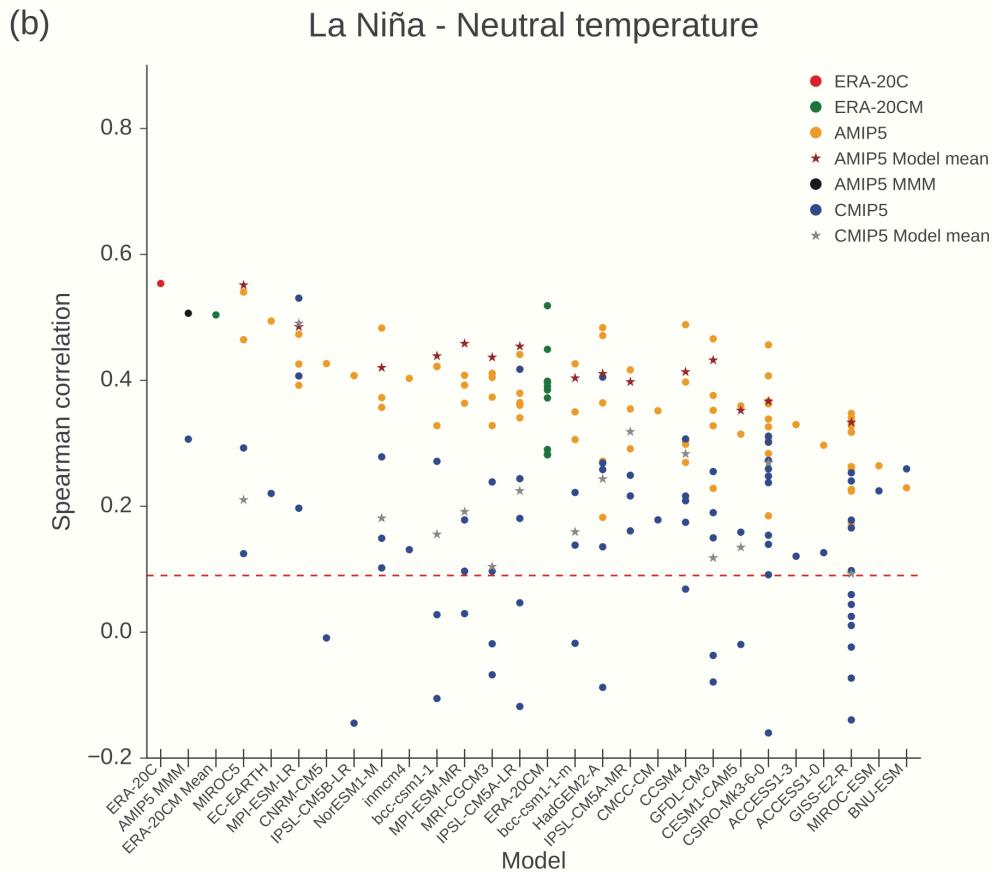
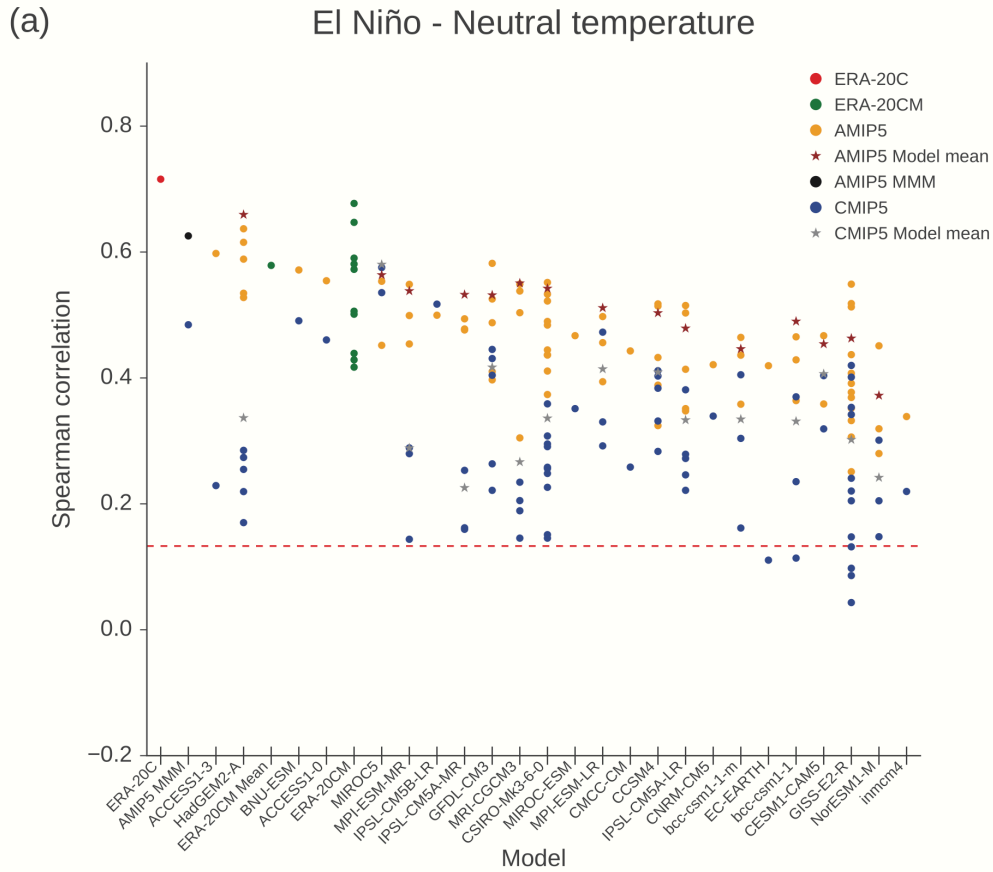


1000 **Fig 6:** El Niño (a) and La Niña (b) pattern correlations of precipitation anomalies between  
1001 40°N - 40°S during 1945-2005 against CRU. CMIP5 models (blue), ERA-20CM (green) and  
1002 ERA-20C (red) are ordered on the x-axis left to right by the average of their correlations.  
1003 Grey triangles represent the same composite patterns correlated to ERA-20C. Individual  
1004 model ensemble averages are shown by yellow stars, and the CMIP5 multi-model ensemble  
1005 mean (using the individual model ensemble means from models with multiple realisations  
1006 and single realisations from models providing only one simulation) by the black filled circle.  
1007 The red dotted lines represent the threshold at which correlations are statistically significant  
1008 at the 5% level.  
1009



1010

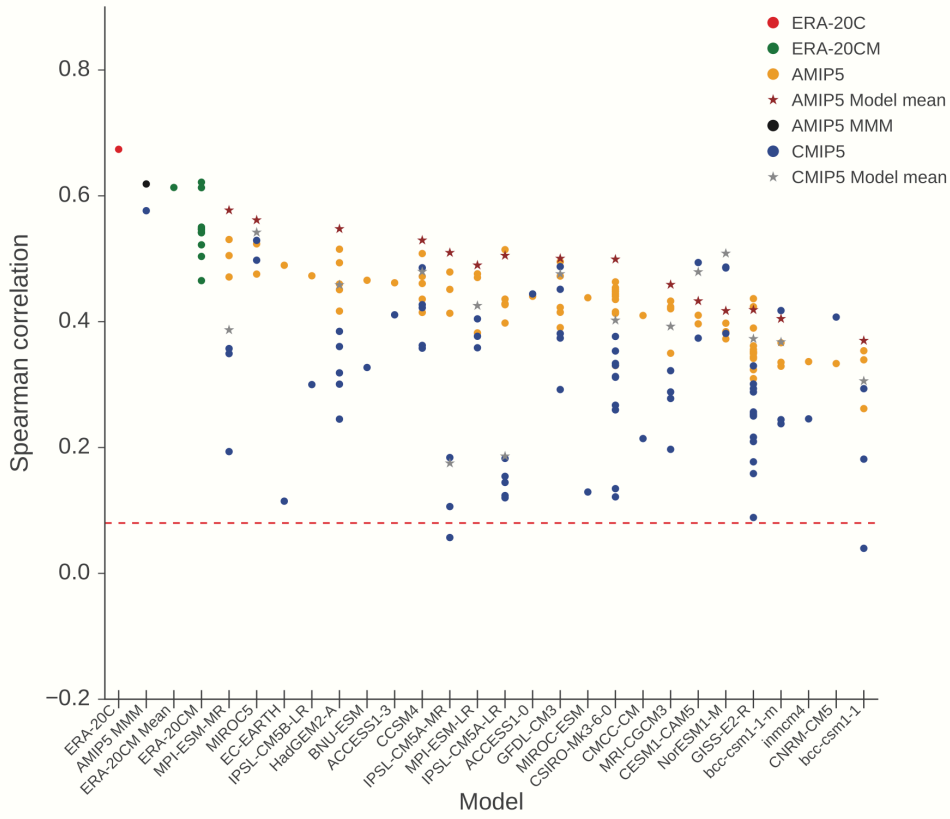
1011 **Fig 7:** Scatterplots between temperature (x-axis) and precipitation (y-axis) anomaly pattern  
 1012 correlations for El Niño (a) and La Niña (b) phases. Each dot represents a member of the  
 1013 CMIP5 multi-model ensemble. The blue line of best fit is a linear least-squares regression. A  
 1014 large regression coefficient between x-axis and y-axis suggests that CMIP5 models that  
 1015 simulate well ENSO temperature teleconnections also represent well ENSO precipitation  
 1016 response.



1018 **Fig 8:** El Niño (a) and La Niña (b) pattern correlations of temperature anomalies between  
1019 40°N - 40°S during 1979-2005 against CRU. AMIP runs (yellow), CMIP5 (blue), ERA-  
1020 20CM (green) and ERA-20C (red) are ordered on the x-axis left to right by the average of  
1021 their correlations. Individual model ensemble averages are shown by red stars (AMIP) and  
1022 grey stars (CMIP), and the AMIP/CMIP5 multi-model ensemble means (using the individual  
1023 model ensemble means from models with multiple realisations and single realisations from  
1024 models providing only one simulation) by the black/blue filled circle in the *AMIP5 MMM*  
1025 column. The red dotted lines represent the threshold at which correlations are statistically  
1026 significant at the 5% level.  
1027

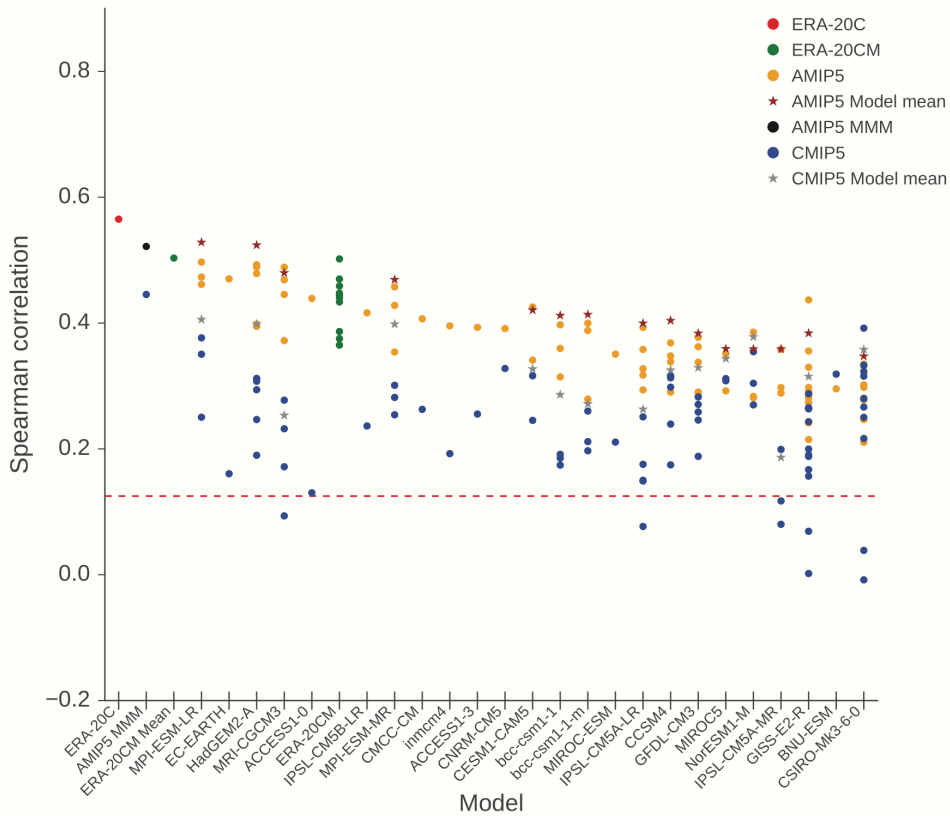
(a)

### El Niño - Neutral rainfall

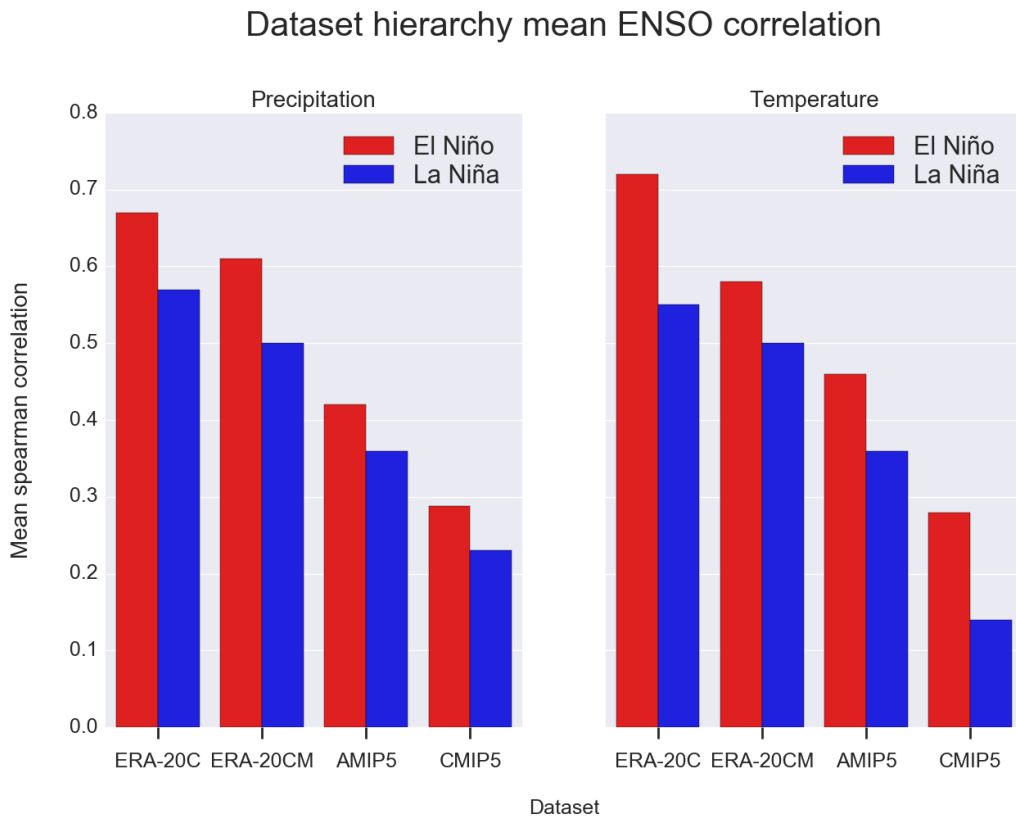


(b)

### La Niña - Neutral rainfall

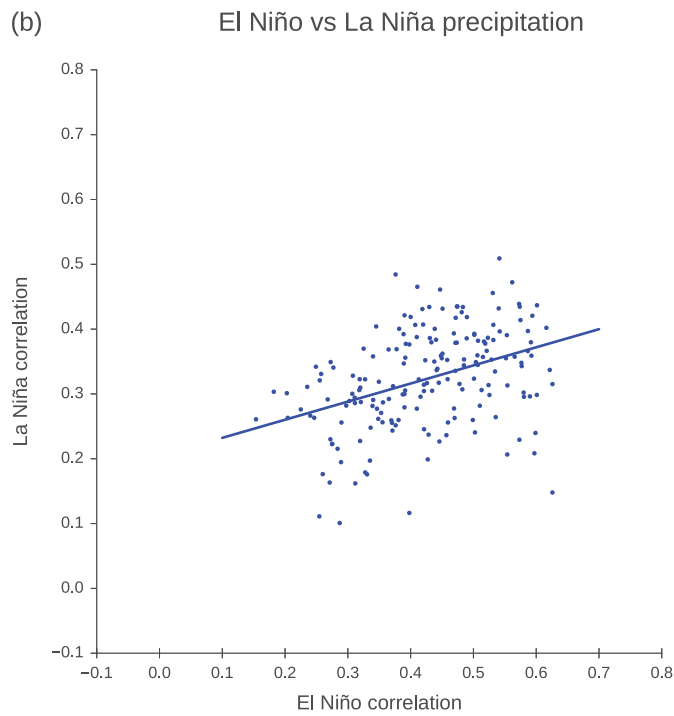
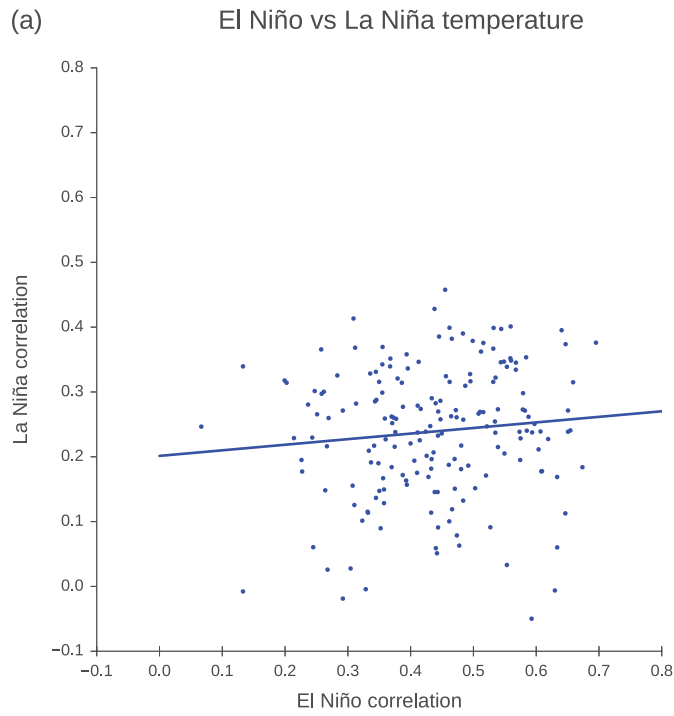


1029 **Fig 9:** El Niño (a) and La Niña (b) pattern correlations of precipitation anomalies between  
1030 40°N - 40°S during 1979-2005 against CRU. AMIP runs (yellow), CMIP5 (blue), ERA-  
1031 20CM (green) and ERA-20C (red) are ordered on the x-axis left to right by the average of  
1032 their correlations. Individual model ensemble averages are shown by red stars (AMIP) and  
1033 grey stars (CMIP), and the AMIP/CMIP5 multi-model ensemble means (using the individual  
1034 model ensemble means from models with multiple realisations and single realisations from  
1035 models providing only one simulation) by the black/blue filled circle in the *AMIP5 MMM*  
1036 column. The red dotted lines represent the threshold at which correlations are statistically  
1037 significant at the 5% level.  
1038



1039  
 1040  
 1041  
 1042  
 1043  
 1044  
 1045  
 1046  
 1047  
 1048  
 1049  
 1050  
 1051  
 1052

**Fig 10:** Summary of El Niño (red) and La Niña (blue) teleconnection pattern agreements. Correlations represent the average pattern correlation of temperature (right) and precipitation (left) anomalies against CRU for each group of data with different observational constraints (i.e. ERA-20C, ERA-20CM, SST-prescribed AMIP5, and fully-coupled CMIP5 simulations). Based on results in Figures 8 and 9 (i.e. for the data period 1979-2005).



1053

1054

**Fig 11:** CMIP5 El Niño (x-axis) against La Niña (y-axis) anomaly pattern spearman

1055

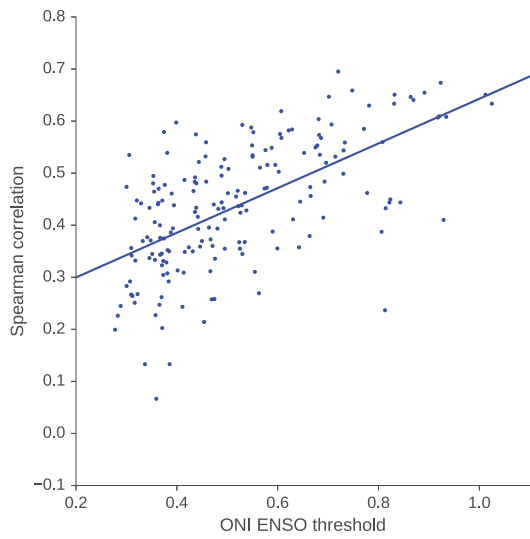
correlations for temperature (top) and precipitation (bottom). The blue line is a linear least-

1056

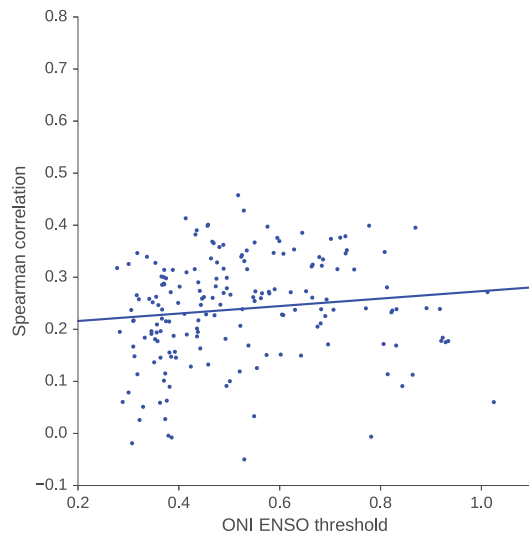
squares regression.

1057

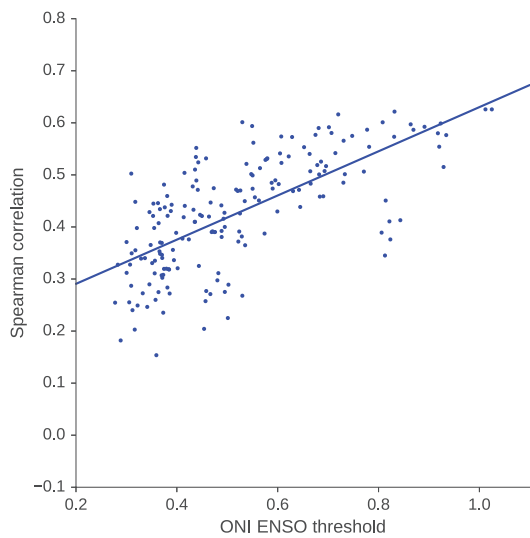
(a) El Niño-Neutral temperature vs SST variability



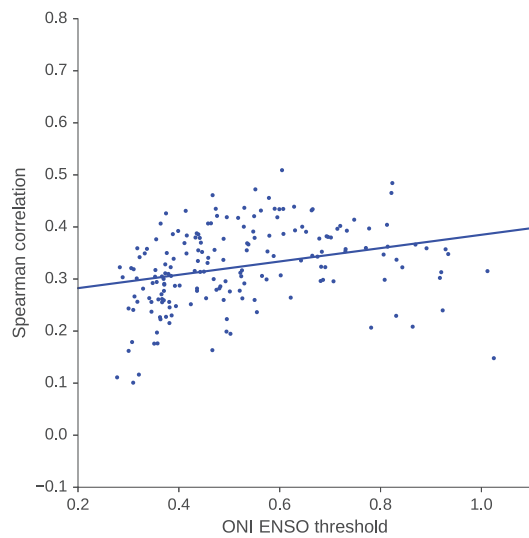
(b) La Niña-Neutral temperature vs SST variability



(c) El Niño-Neutral precipitation vs SST variability



(d) La Niña-Neutral precipitation vs SST variability



1058

1059

1060

1061

1062

1063

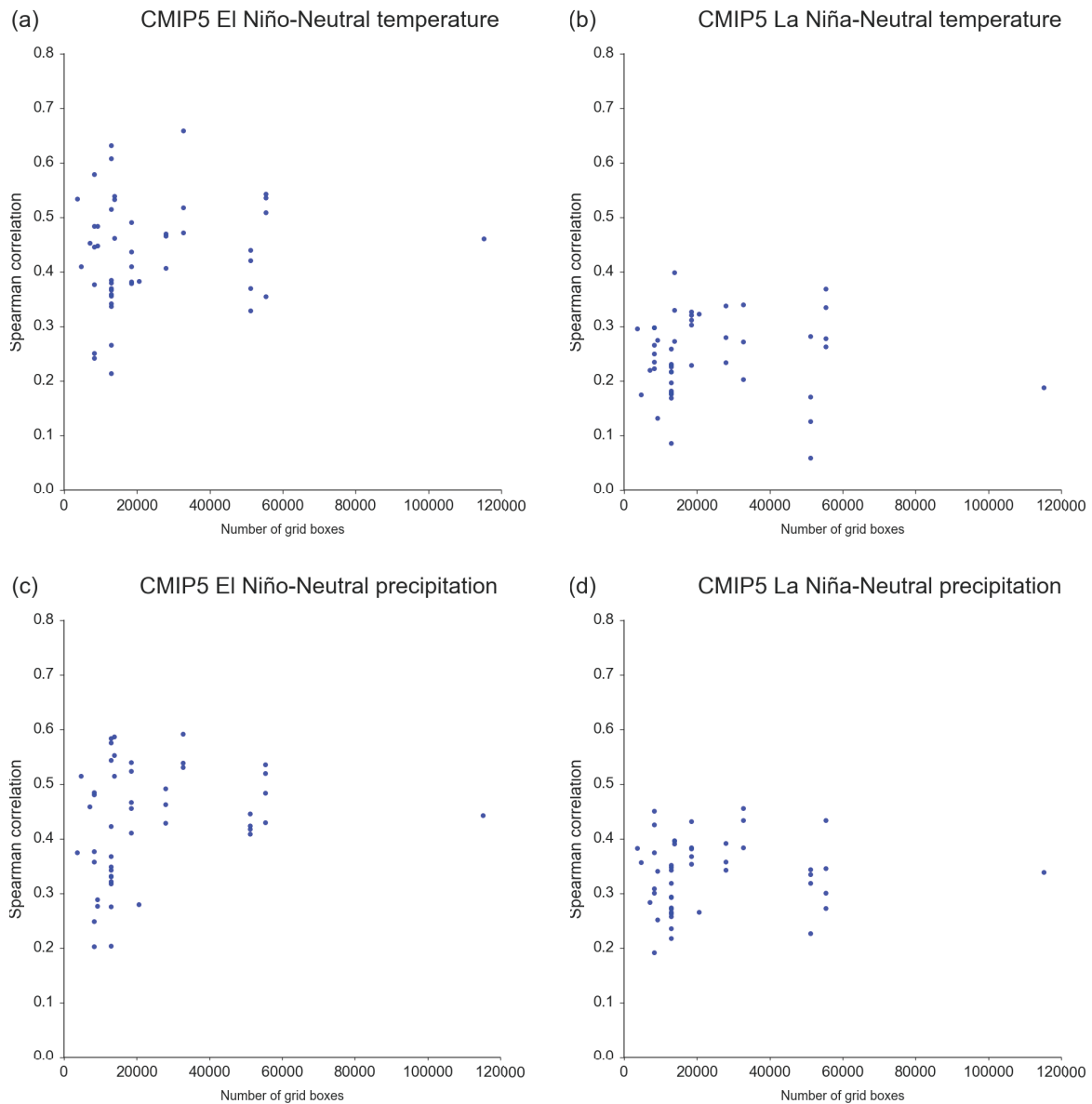
1064

1065

1066

1067

**Fig 12:** Scatterplot of the CMIP5 ONI ENSO thresholds (x-axis) against spearman correlations (y-axis) of temperature (top row) and precipitation (bottom row) anomaly patterns against CRU during El Niño (left column) and La Niña (right column). Each blue dot represents a model run. A line of best fit is drawn using linear least-squares regression. The ONI threshold of each model run is used here as an indication of ENSO variability in the model. Overall, models with larger ENSO variability tend to have a more realistic representation of El Niño teleconnections. The relationship is weaker for the La Niña counterpart.



1068

1069

1070

**Fig 13:** Scatterplot of the average spearman correlation of each CMIP5 model's runs

1071

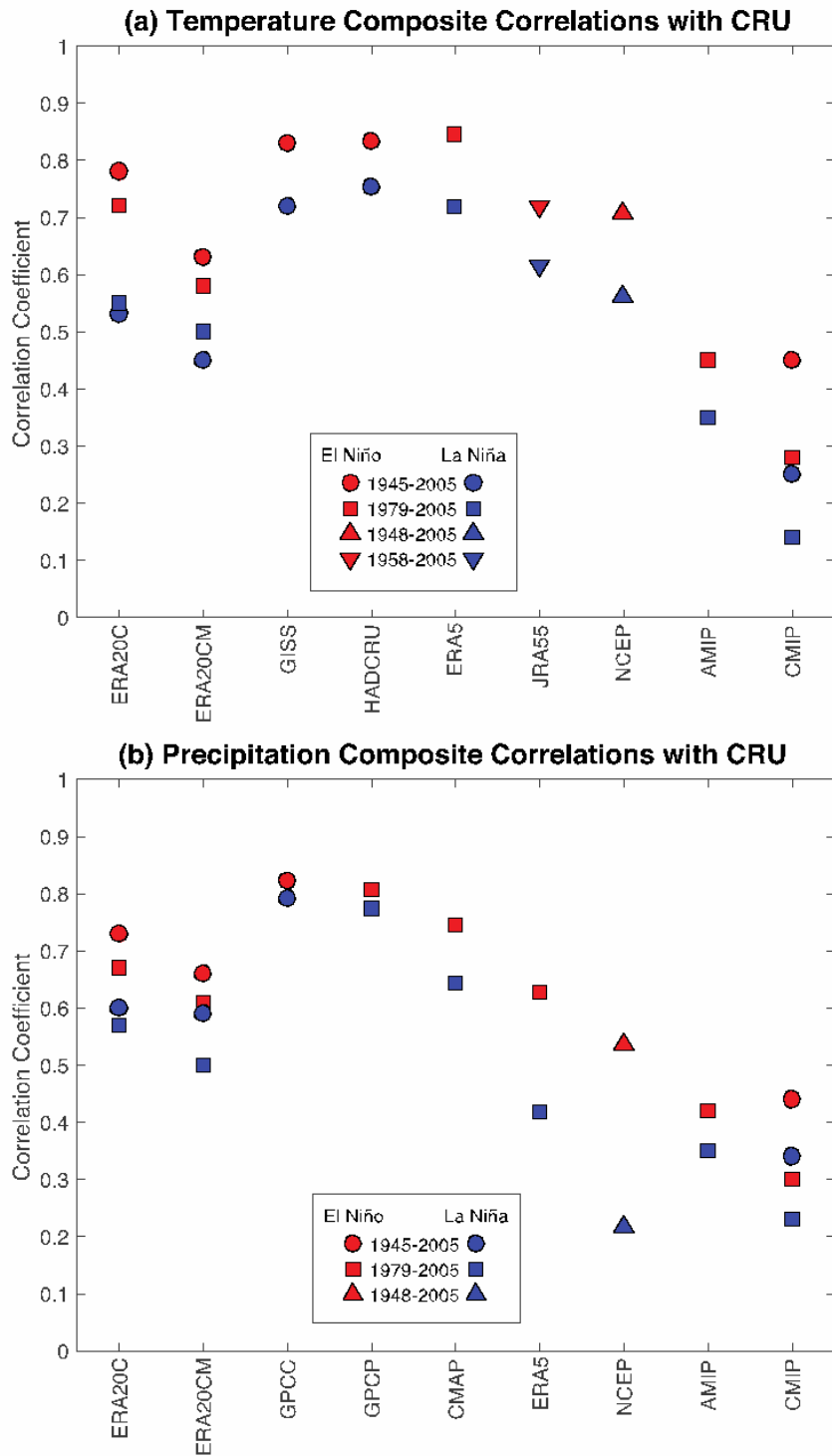
measured against the model's original number of grid boxes. Correlations represent

1072

temperature (top row) and precipitation (bottom row) anomalies during El Niño (left column)

1073

and La Niña (right column).



1074

1075

**Fig 14:** Correlation coefficients of (a) temperature and (b) precipitation anomaly patterns

1076

between 40°N - 40°S during El Niño (red symbols) and La Niña (blue symbols) for

1077

observations (GISS, HadCRUT, GPCC, GPCP and CMAP), reanalysis (ERA20C,

1078

ERA20CM, ERA5, JRA55 and NCEP), AMIP and CMIP models, against the observational

1079

reference CRU. Note datasets have different time periods.

1080